Perseverance rover reveals ancient delta-lake system and flood deposits at Jezero crater, Mars

N. Mangold, S Gupta, O Gasnault, G Dromart, J D Tarnas, S F Sholes, B Horgan, C Quantin- Nataf, A J Brown, S. Le Mouélic, et al.

Perseverance rover reveals ancient delta-lake system and flood deposits at Jezero crater, Mars

N. Mangold[1*], S. Gupta[2], O. Gasnault[3], G. Dromart[4], J. D. Tarnas[5], S. F. Sholes[5], B. Horgan[6], C. Quantin-Nataf[4], A. J. Brown[7], S. Le Mouélic[1], R. A. Yingst[8], J. F. Bell[9], O. Beyssac[10], T. Bosak[11], F. Calef III[5], B. L. Ehlmann[12], K. A. Farley[12], J. P. Grotzinger[12], K. Hickman-Lewis[13,14], S. Holm-Alwmark[15,16,17], L. C. Kah[18], J. Martinez-Frias[19], S. M. McLennan[20], S. Maurice[3], J. I. Nuñez[21], A. M. Ollila[22], P. Pilleri[3], J. W. Rice Jr[8], M. Rice[23], J. I. Simon[24], D. L. Shuster[25], K. M. Stack[5], V. Z. Sun[5], A. H. Treiman[26], B. P. Weiss[5,11], R. C. Wiens[22], A. J. Williams[27], N. R. Williams[5], K. H. Williford[5,28]

1 Laboratoire Planétologie et Géodynamique, Centre National de Recherches Scientifiques, Université Nantes, Université Angers, Unité Mixte de Recherche 6112, 44322 Nantes, France.

2 Department of Earth Science and Engineering, Imperial College London, London SW7 2AZ, UK.

3 Institut de Recherche en Astrophysique et Planétologie, Université de Toulouse, Université Paul Sabatier, Centre National de Recherches Scientifiques, Observatoire Midi-Pyrénées, 31400 Toulouse, France.

4 Laboratoire de Géologie de Lyon-Terre Planètes Environnement, Univ Lyon, Université Claude Bernard Lyon 1, Ecole Normale Supérieure Lyon, Centre National de Recherches Scientifiques, 69622 Villeurbanne, France.

5 Jet Propulsion Laboratory, California Institute of Technology, Pasadena, CA 91109, USA.

6 Earth, Atmospheric, and Planetary Sciences, Purdue University, West Lafayette, IN 47907, USA.

7 Plancius Research, Severna Park, MD 21146, USA.

8 Planetary Science Institute, Tucson, AZ 85719, USA.

9 School of Earth and Space Exploration, Arizona State University, Tempe, AZ 85287, USA.

10 Institut de Minéralogie, de Physique des Matériaux et de Cosmochimie, Unité Mixte de Recherche 7590, Centre National de Recherches Scientifiques, Sorbonne Université, Museum National d'Histoires Naturelles, 75005 Paris, France.

11 Department of Earth, Atmospheric, and Planetary Science, Massachusetts Institute of Technology, Cambridge, MA 02139, USA.

12 Division of Geological and Planetary Sciences, California Institute of Technology, Pasadena, CA 91125, USA.

13 Department of Earth Sciences, The Natural History Museum, Cromwell Road, South Kensington, London, SW75BD, United Kingdom.

14 Dipartimento di Scienze Biologiche, Geologiche e Ambientali, Università di Bologna, I-40126, Italy.

15 Niels Bohr Institute, University of Copenhagen, 2100 Copenhagen, Denmark.

16 Department of Geology, Lund University, 22362 Lund, Sweden.

17 Natural History Museum of Denmark, University of Copenhagen, 1350 Copenhagen, Denmark.

18 Department of Earth and Planetary Sciences, University of Tennessee, Knoxville, TN 37996, USA.

19 Instituto de Geociencias, Consejo Superior de Investigaciones Cientificas, Universidad Complutense Madrid, 28040 Madrid, Spain.

20 Department of Geosciences, Stony Brook University, Stony Brook, NY 11794, USA.

21 Johns Hopkins University Applied Physics Laboratory, Laurel, MD 20723, USA.

22 Space & Planetary Exploration Team, Los Alamos National Laboratory, Los Alamos, NM 87545, USA.

23 Geology Department, College of Science and Engineering, Western Washington University, WA 98225, USA.

24 Center for Isotope Cosmochemistry and Geochronology, Astromaterials Research and Exploration Science, NASA Johnson Space Center, Houston, TX 77058, USA.

25 Dept. Earth and Planetary Science, University of California, Berkeley, CA 94720, USA.

26 Lunar and Planetary Institute, Universities Space Research Association, Houston, TX 77058, USA.

27 Department of Geological Sciences, University of Florida, Gainesville, FL 32611, USA.

28 Blue Marble Space Institute of Science, Seattle, WA 98104, USA

* Correspondence to Nicolas Mangold: nicolas.mangold@univ-nantes.fr

Abstract

Observations from orbital spacecraft have shown that Jezero crater, Mars, contains a prominent fan-shaped body of sedimentary rock deposited at its western margin. The Perseverance rover landed in Jezero crater in February 2021. We analyze images taken by the rover early in the mission, finding that the fan has outcrop faces that were invisible from orbit, which record the hydrological evolution of Jezero crater. We interpret the presence of inclined strata in these outcrops as evidence for deltas that advanced into a lake. By contrast, the uppermost fan strata are composed of boulder conglomerates, which imply deposition by episodic high-energy floods. This sedimentary succession indicates a transition from a sustained hydrologic activity in a persistent lake environment to highly energetic, short-duration fluvial flows.

Mars is currently cold and hyper-arid; liquid water is not stable at its surface. However, orbital and rover observations of features including valley networks, sedimentary fans and ancient lake beds indicate the planet once had a warmer, wetter climate (*1-3*). Uncertainties remain about the character, timing and persistence of aqueous activity (and therefore potential habitability) on early Mars. The Mars 2020 mission, whose main component is the Perseverance rover, is the first step in a planned multi-mission campaign to return Martian samples to Earth and examine them for potential biosignatures (*4*). The 45-km diameter Jezero crater was selected as the landing site based on orbital images, which showed geomorphic expressions of two sedimentary fan structures (western and northern) at the edges of the crater (*5-6*). These were inferred to be river delta deposits that formed in an ancient lake basin during the Late Noachian or Early Hesperian epochs on Mars (~3.6-3.8 Ga) (*5-9*) (Fig. 1, Fig. S1). Spectroscopic observations from orbit have detected phyllosilicates and carbonates, minerals indicative of past aqueous environments (*6, 7, 10*). Rover investigations on the surface could provide insight into the evolution of Jezero's ancient lake system and the timescale of liquid water residence on the surface.

The Perseverance rover landed on the floor of Jezero crater on 18 February 2021. The landing site, informally named "Octavia E. Butler", is ~2.2 km from the SE-facing erosional scarp of the western fan deposits, an important target for the mission (Fig. 1, Fig. S1-S5). During the first three months of the mission, we obtained images of the western fan using the Mastcam-Z camera and the Remote Micro-Imager (RMI) of the SuperCam instrument (*11-14*) (Fig. 1-4, Fig. S2-S4, Fig. S6-S7, Tab. S1-S2). We use these long-distance images to investigate the stratigraphy and sedimentary characteristics of the fan deposits, and interpret their implications for the ancient lake in Jezero crater.

Kodiak butte

Images of a prominent butte (an isolated flat-topped hill), which we informally named Kodiak, ~1 km south of the main fan deposit (Fig. 1), provide insight into sedimentary processes at Jezero crater. We interpret it as an erosional remnant of an originally more extensive fan deposit, due to the morphological similarity of Kodiak butte to the main fan exposures, and the near identical elevation of its top (*15*). A mosaic of the ESE-facing wall of Kodiak (Fig. 1-2, Fig. S2) shows two main outcrop areas with three distinct sedimentary layer types: a series of inclined strata sandwiched between layers comprised of horizontal strata, described in detail below. There is no evidence for later dislodgement or rotation of blocks, such as faults or slippage, and therefore we interpret the observed stratigraphy as reflecting the original depositional geometry.

Kodiak butte consists of two outcrop sections that expose five distinct stratigraphic bodies, which we designate k1 to k5 (Fig. 2). The unit k1 is 17 m thick vertically and extends horizontally at least 70 m to the northern butte margin visible from Perseverance (Fig. 2A-C). The lowest visible part of k1 consists of plane-parallel horizontal to low-angle thinly bedded strata. These show recessive weathering, characteristic of readily eroded fine-grained lithologies (mudstones or sandstones). Overlying these is a ~10 m thick series of strata comprised of steeply inclined beds with apparently southward dips at angles up to 35˚. Individual beds, defined by variations in erosion, have apparent thicknesses from 10 to 50 cm. We infer their primary lithology to be finer-grained than a conglomerate, possibly sandstone, with scattered cobbles. A second unit of dipping strata (k2, 3 m thick) immediately overlies the uppermost strata of k1.

In the southern portion of Kodiak, sedimentary units (k3, 13 m thick) and (k4, 10 m thick) show similar geometries to those in k1 (Fig. 2D-F). In its lower section, k3 consists of thinly bedded, gently dipping, and horizontal strata. These show recessive weathering, again indicating mudstones or sandstones. These pass upwards into a distinct 7-m-thick section of inclined beds that dip consistently to the south. Locally, these dipping beds contain isolated boulders and cobbles (up to 40 cm in diameter, Fig. 2F). At their base, these beds show a downward asymptotic decrease in inclination and pass into lowermost horizontal strata. Overlying the inclined beds across a sharp sub-horizontal truncation surface, k4 shows low-angle to locally cross-stratified sub-horizontal strata. The overlying unit k5 erosionally truncates k4 (Fig. 2E). Unit k5 consists of unsorted conglomerates, which contain boulders up to 1.5 meter in long axis, implying a marked change in depositional regime.

Inclined beds in k1 display a downward asymptotic decrease in apparent dip angle and pass gradually into underlying gently dipping and horizontal strata (Fig. 2). At the top, the transition from inclined beds to sub-horizontal beds also shows a gradual change in dip (Fig. 2C). This geometric arrangement of strata shows that k1 consists of a single depositional unit with a tripartite architecture in which the lower gently dipping beds are defined as bottomsets, the inclined beds as foresets and the uppermost horizontal layers as topsets. Similar to k1, we interpret the k3 inclined beds to be foresets that pass downward, with decreasing apparent dip angle into subhorizontal strata we interpret as bottomsets. Overlying k3, subhorizontal strata of k4 then represent topsets. The sharp discontinuity between k3 and k4 is distinct from that observed in k1 where the transition appears to be continuous.

We interpret this distinct tripartite bedding geometry (bottomsets, foresets and topsets) of the units k1to k4 as representing deposition in steeply fronted Gilbert-type deltas (supplementary text, Fig. S8) (*16, 17*). The thicknesses and lateral extents (>70 m) of the foreset units are too great to be explained by formation as dunes formed by underwater currents or as lateral accretion deposits in fluvial bars. The presence of cobbles and boulders in the foreset strata (Fig. 2F) is inconsistent with their formation as aeolian dunes. In a Gilbert delta, topset strata are fluvial deposits formed in delta top environments. The foreset strata represent deposits formed by gravity-driven flow processes on steeply dipping delta fronts. Bottomset strata represent finer-grained sediments deposited in areas immediately lakeward of the delta front. The transition from topset to foreset (the topset breakpoint) constrains the lake level at the time of deposition. The thickness of the foreset units provides a lower limit of 10 m water depth in this portion of the Jezero lake basin at that time. The bases of topset strata in units k1 and k4 are respectively at ca. -2500 m and -2490 m elevation (below the reference equipotential), corresponding to past lake levels at the time of deposition (Fig. 5).

Elevation differences suggest that units k3 and k4 are stratigraphically higher, and hence younger, than k1 (Fig. 2). Examination of the exposures on both faces of the butte indicates a similar architecture with two differences: a discontinuity above k3 foresets (not present in k1), and the presence of the terminal boulder-rich unit k5 that truncates k4 topsets (absent above k1 or k2). These differences indicate that k1-k2 units on one side of the scarp, and k3-k4 units on the other

side, are not the same stack of layers (Fig. S2). This rules out the possibility of a fault being the explanation for the offset in elevation.

The orientation of foresets indicate an apparent southward progradation in this sector of the western fan (i.e., the delta advanced toward the south) during episodes of stationary or slowly decreasing lake level. The sub-horizontal topset truncation of underlying foreset units between k3 and k4 may reflect a drop in lake level. In contrast, the stacking of delta units k1-k3 stratigraphically on top of one another indicates an overall lake level rise of ~10 m before the truncation by k4. Thus, the observed geometries in Kodiak indicate delta growth into a lake system with fluctuating lake levels.

Previous studies have proposed that Jezero crater hosted an open-lake system with the water level at an elevation of -2395 m (*5*); this inference is derived from the observations that the inlet valley (feeding the western fan) and the breaching valley (that dissects the eastern rim of the crater) have approximately the same elevation of -2395 m. However, our results indicate that the lake level during deposition of units k1 to k4 (ca. -2500 m and -2490 m) was ~100 m below the inferred open-system lake level (Fig. 5). Thus, Jezero lake was closed (no outlet river) at the time of the delta progradation at Kodiak, which is a hydrological system conducive to short-term fluctuations in the lake level. Nevertheless, the overall stratigraphy indicates progradation of the western delta system and long-term lake level regression.

The western fan

Images of the SE-facing erosional front of the western fan expose sedimentary geometries within the uppermost fan deposits at several locations, at the top of ~60 m tall scree-covered hillslopes (Fig. 1, Fig. S3-S5). In a RMI mosaic (Fig. 3), the upper section of the northernmost hillslope exposes three sedimentary bodies (a1 to a3) that consist of conglomerates and finer-grained rocks (the grain size is not resolved). The lowermost unit a1 has an apparent thickness of 7 m and is composed of 10 to 30 cm thick tabular-bedded strata, which show an apparent dip to the SW. At its northern margin, a1 exhibits steeply inclined beds (up to 30°, Fig. 3D) that likely represent either lateral accretion sets formed in a large fluvial channel bar, or delta foresets.

A distinct coarse-grained lenticular unit a2 overlies a1; it is approximately 30 m wide and asymmetric with a maximum thickness of 9 m at its southern edge, thinning to less than a meter to the north. Unit a2 is dominated by unsorted, clast-supported conglomerates of cobbles and boulders (Fig. 3C). The deposit is structureless locally displaying faint layering. Clasts show no preferred orientation or size segregation visible in images. The largest boulder, ~1.5 m on its long axis, casts a shadow below it, implying that it is embedded in the outcrop, so did not roll down from the upper slope. A shape assessment of 24 boulders shows that 13 are rounded and 11 are angular (*14*). Size measurements of 333 boulders/cobbles (Fig. S6-7) indicate a distribution with a median size (D_{50}) of 16.4±2.2 cm and a D_{84} (84% of clasts are smaller) of 25.9±2.2 cm (Fig. 3E) (*14*).

We infer that unit a2 was deposited from rapidly decelerating high velocity flood flows that can transport boulders, based on its lack of sorting, large clast sizes, absence of well-developed stratification, and disorganized but clast-supported fabric. This interpretation is based on well constrained observations of flood deposits on Earth (*18, 19*). The rounding of some of the largest

clasts indicates that they have undergone abrasion by collisional processes during fluvial transport. The lens-like shape of the conglomerate body a2 suggests that it is a channel fill. Assuming its dimensions represent the formative fluvial channel, the channel was 3-10 meters deep. We estimate discharge rates using two methods: a Mars-modified version of the Darcy-Weisbach equations for river flows (*20, 21*) and the velocity threshold necessary to lift up the largest clasts observed (*14*). Both methods give consistent results with velocities of 1.6 to 8.6 m s^{-1} and discharge rates of 70 to 3000 $m^3 s^{-1}$ (Tab. S3) (*14*).

Unit a3 overlies a2; a3 is generally finer-grained than a2, up to 10 m thick, and extends ~80 m laterally. Unit a3 shows horizontal to low angle stratification, with some local cross-stratification. Unit a3 contains isolated cobbles and boulders; including a 50 cm diameter boulder that is being eroded from the outcrop (Fig. 3C). Based on the presence of planar stratification and cross-stratification, we infer unit a3 to be a sandstone with outsized clasts. If the a2-a3 contact is gradational, then these units are part of the same depositional sequence and a3 may record the waning stage of the fluvial flood flow. Alternatively, a3 could represent a second, lower energy event in which the flux of boulders was reduced.

Stratigraphic relationships between a1-a3 and underlying units are not well constrained because the exposure is debris-covered (Fig. 1G). However, the lowest part of the hillslope does expose one set of beds that are inclined to the east (Fig. 1G). The inclined beds could be either delta foresets, as observed at Kodiak and hypothesized from orbital images (*22, 23*), or they could represent a landslide block, as their dip is similar to the local slope.

Additional coarse-grained deposits are visible at scarps b to d (Fig. 1, Fig. S5). Scarp b is a 15 m tall cliff that exposes two distinct sedimentary bodies (Fig. 1C-D, Fig. 4). The lower unit comprises 10 to 40 cm thick parallel planar sub-horizontal beds b1, which we infer to consist of sedimentary rocks that are finer-grained than conglomerate. Unit b1 is overlain by a unit b2, a conglomerate of unsorted cobbles and boulders (Fig. 4C) with varying degrees of rounding. Unit b2 shows faint inclined bedding (Fig. 4) and truncates unit b1 at a discontinuous, scoured contact at its base. The scarps at locations c and d (Fig. 1E-F) expose units like those at b, with sub-horizontal finer-grained strata overlain by coarser-grained, likely cobble-boulder conglomerates. The stratal geometry shown by these outcrops is similar to that observed in the uppermost section at Kodiak k5. Sub-horizontal strata such as b1 could then represent delta topsets similar to k4.

The unconsolidated boulder-rich deposits observed at the scarp tops contain many rounded, scattered boulders (Fig. S9-S10, supplementary text). We interpret these unconsolidated disorganized deposits as residual lags resulting from weathering of underlying boulder conglomerates and sandstones (Fig. 3). Comparison with geological maps constructed from orbital images (*14*) indicates that these unconsolidated deposits are part of the Delta Blocky unit, which comprises much of the upper surface of the western fan and is defined by positive relief elongate ridges and the presence of numerous clasts. This unit has previously been interpreted as inverted fluvial channel-belt deposits (*8, 15, 22, 23*) (Fig. S1). Based on our rover images, we interpret the boulder-bearing units a2-a3, b2 and k5 as fluvial deposits that represent locally preserved sections from these well-developed fluvial channel-belt deposits.

We use orbital and multi-spectral Mastcam-Z observations of the western fan exposures to investigate the mineralogy and provenance of the boulder conglomerates (Fig. S11-S12, supplementary text). These data indicate that the boulder conglomerates and the blocky deposits

are dominated by low calcium pyroxene (LCP), unlike other sections of the fan stratigraphy which are dominated by phyllosilicates and olivine (Fig. S11). This interpretation is consistent with the source of the boulders/cobbles as being either the LCP-bearing crater rim of Jezero, and/or the widespread exposures of LCP-rich crust >60 km upstream of Jezero crater (Fig S11) (*7, 24*). An igneous rock source would be consistent with the boulders' massive shape and apparent lack of internal fabric. Substantial transport distances from distant sources is consistent with the presence of rounded boulders *(14, 25*), whereas the source of angular boulders could be more proximal, such as the crater rim.

Implications for hydrologic evolution and sample return

Our rover images constrain the hydrologic evolution of Jezero crater, and potentially wider early Mars climate and habitability. The delta architecture at Kodiak indicates deposition in a closed lake system, under fluctuating water levels and changing styles of flow during later stages. This indicates that the climate on Mars at that period (late Noachian or early Hesperian) was warm and humid enough to support a hydrologic cycle on the martian surface, at least episodically.

The presence of coarse-grained material (cobbles and boulders) in steep foresets is characteristic of Gilbert-type deltas prograding into deep lake systems (*16, 26, 27*) (Fig. S6). The highest lake elevation recorded by the transition from topsets to foresets at Kodiak has an altitude of about -2490 m (Fig. 5), well below the lake levels previously proposed of -2395 m and -2250 m based on the basin topography (*5, 23, 28*). The Kodiak delta deposits are located 5 km away from the outlet, and they correspond to a regression to lower lake levels because they formed after a large part of the delta was already deposited. Our results do not exclude periods of higher standing lake levels in the crater, but do imply that any such periods occurred prior to the one recorded at Kodiak. Our observations of Kodiak indicate that the delta front extended ~1 km further south than the main western fan scarp. Delta deposits could have originally extended further eastwards as well.

The boulder conglomerates in units a2, b2 and k5 (Fig. 1) indicate repeated flood episodes of variable intensities. These deposits are distinct from the low- to moderate-energy fluvial deposits characteristic of river-dominated deltas (*19*). Their stratigraphic positions overlying delta deposits indicate that they are also unlikely to be sediment gravity flow deposits formed in a deep lacustrine setting. We cannot determine whether the boulder conglomerates were deposited when a lake still existed in Jezero crater. Their geometry is consistent with fluvial deposits on Earth that show downstream transition to gravel-to-sand Gilbert-type underwater foresets (*29*). The lowermost boulder conglomerates we observe are at an elevation of about -2490 m, similar to that of the lake level deduced from foresets at Kodiak. Therefore, these fluvial floods could have formed when the lake was around this level, or at a lower level. Alternatively, the widespread boulder conglomerate deposits could represent a younger depositional system that overlies deltaic strata.

Our results indicate a temporal transition in the energy regime of fluvial systems feeding the western fan, from sustained fluvial activity that built delta deposits prograding into the Jezero crater lake, to episodes characterized by high discharge fluvial flows capable of mobilizing meter-scale boulders over potentially tens of km transport distances. Sub-horizontal topset beds at Kodiak (and possibly b1) are relatively homogenous deposits compared to the boulder conglomerates, and are likely sandstones, consistent with deposition by sandy rivers. The presence of occasional boulders in the Kodiak foresets points to locally higher intensity flow conditions, but the boulder

conglomerate units record much higher magnitude flood episodes. Local discharge rate estimates (70 to 3000 $m^3.s^{-1}$) for the floods are consistent with those previously estimated from braided fluvial channels observed upstream in Neretva Vallis (*9*). Nevertheless, these are late-stage deposits formed from more intermittent, energetic flows than the topsets which they overlie, so discharge rates cannot be used to estimate the formation time needed of the entire delta fan.

The mechanism responsible for the flood events is unknown. The presence of rounded boulders demonstrates that substantial abrasion of clasts occurred during fluvial transport. This evidence, coupled with the presence of multiple flood episodes with similar boulder sizes as in unit a2, exclude megafloods such as those proposed for martian outflow channels (*30*). Flood episodes could have formed by a variety of processes (*18, 31*) such as intense rainfall events, rapid snowmelt episodes (from either a climatic origin (*1, 3*) or heating by volcanism or impact (*32, 33*)), or through progressive building of glaciers and glacial lakes in the watershed creating episodic surges (*31*). Thus, the transition in flow intensity at Jezero crater may be related either to paleoclimatic shifts (global or regional), or changes in watershed hydrology.

The Jezero crater deposits provide information which could be extrapolated to other paleolakes on Mars (*2, 26, 34*). Favorable climatic conditions for rivers and lakes are already known to have also been present at Gale crater (*2, 35*). However, the conglomerates in Jezero crater require much higher energy environments than those in Gale crater, where the median clast size is <1 cm and the largest clasts are <10 cm (*35*) (Fig. 3E). A transition to drier conditions at Gale crater has been suggested to explain a change in mineralogy from clay- to sulfate-bearing minerals, and alternating eolian and fluvial deposits (*36, 37*). However, in Gale crater no fluvial flood deposits have been observed stratigraphically overlying the lacustrine deposits of the Murray formation (*2*), contrasting with the hydrologic evolution of Jezero crater.

Our results inform sampling strategies by Perseverance in Jezero crater (supplementary text). First, boulders >1 m in diameter provide an opportunity to analyze and collect samples from crustal rocks sourced from outside Jezero that must predate the rocks within the crater (*4, 24*). These likely contain records of the ancient Martian interior. Second, the finer-grained bottomset strata, which are known from orbital data to contain Fe/Mg smectite clays (*6, 7, 10*), have high potential to preserve organic matter or potential biosignatures (*38-40*).

References

(1) R.A. Craddock, A.D. Howard, The case for rainfall on a warm, wet early Mars. *J. Geophys. Res*. **107**, 5111 (2002).

(2) J.P. Grotzinger *et al.*, Deposition, exhumation, and paleoclimate of an ancient lake deposit, Gale crater, Mars. *Science* **350**, aac7575 (2015).

(3) R. Wordsworth *et al.* A coupled stochastic model of the climate and redox evolution of Mars. *Nature Geosci.* **14**, 127-132, 2021.

(4) D. W. Beaty, the iMOST team (2019) The potential science and engineering value of samples delivered to Earth by Mars sample return. *Meteorit. Planet. Sci*. **54**, S3-S152 (2019).

(5) C.I. Fassett, J.W. Head, Fluvial sedimentary deposits on Mars: ancient deltas in a crater lake in the Nili Fossae region. *Geophys. Res. Lett*. **32**, L14201 (2005).

(6) B.L. Ehlmann *et al.* Clay minerals in delta deposits and organic preservation potential on Mars. *Nat. Geosci.* **1**, 355-358 (2008).

(7) T.A. Goudge, J.F. Mustard, J.W. Head, C.I Fassett, S.M. Wiseman,, Assessing the mineralogy of the watershed and fan deposits of the Jezero crater paleolake system, Mars. *J. Geophys. Res.* **120**, 775-808 (2015).

(8) T.A., Goudge, R.A. Milliken, J.W. Head, J.F. Mustard, C.I. Fassett,, Sedimentological evidence for a deltaic origin of the western fan deposit in Jezero crater, Mars and implications for future exploration. *Earth Planet. Sci. Let*. **458**, 357-365 (2017).

(9) N. Mangold *et al.*, Fluvial Regimes, Age and Duration of Jezero Crater Paleolake and its Significance for the 2020 Rover Mission Landing Site, *Astrobiology* **20**, 994-1013 (2020).

(10) B.H. Horgan, R.B. Anderson, G. Dromart, E.S. Amador, M.S. Rice, The mineral diversity of Jezero crater: Evidence for possible lacustrine carbonates. *Icarus* **339**, 113526 (2020).

(11) J.F. Bell III *et al.*, The Mars 2020 Rover Mast Camera Zoom (Mastcam-Z) Multispectral, Stereoscopic Imaging Investigation, *Space Sci. Rev.* **217**, (2020).

(12) S. Maurice *et al.*, The SuperCam instrument suite on the NASA Mars 2020 Rover: Mast Unit and calibration targets, *Space Sci. Rev.* **217**, 47 (2021).

(13) R. Wiens *et al.*, The SuperCam instrument suite on the NASA Mars 2020 Rover: Body Unit. *Space Sci. Rev*. **217**, 4 (2021).

(14) Materials and methods are available as supplementary materials.

(15) K. M. Stack *et al.*, Photogeologic map of the Perseverance Rover field site in Jezero crater constructed by the Mars 2020 Science Team. *Space Sci. Rev.* **216**, 1272020 (2020).

(16) G.K. Gilbert, The topographic features of lake shores. 5th Annual Report. United States Geol. Survey, Washington, D.C., **69–123** (1885).

(17) H. Fayol, Etude sur le terrain houille de Commentry. Bulletin de la Société de l'Industrie Minérale, XV, 543 pp. (1886).

(18) J.E. Costa, Paleohydraulic reconstruction of flash-flood peaks from boulder deposits in the Colorado Front Range. *Geol. Soc. Am. Bull.* **94**, 986-1004 (1983).

(19) M.R. Leeder, Sedimentology: Process and Product (Chapman and Hamm, 344pp., 1982).

(20) E.S. Kleinhans, Flow discharge and sediment transport model for estimating a minimum timescale of hydrological activity of channel and delta formation on Mars, *J. Geophys. Res.* **110**, E12003 (2005).

(21) L. Wilson, G.J. Ghatan, J.W. Head III, K.L. Mitchell, Mars Outflow channels : A reappraisal of the estimation of water flow velocities from water depths, regional slopes and channel floor properties, *J. Geophys. Res.* **109,** E09003 (2004).
(22) T.A. Goudge, D. Mohrig, B.T. Cardena, C.M. Hugues, C.I. Fassett, Stratigraphy and paleohydrology of delta channel deposits, Jezero crater, Mars. *Icarus* **301**, 58-75 (2018).
(23) S.C., Schon, J. W. Head, C.I. Fassett An overfilled lacustrine system and progra-dational delta in Jezero crater, Mars: implications for Noachian climate. *Planet. Space Sci*. **67**, 28–45 (2012).
(24) E. Scheller, B.L. Ehlmann, Composition, stratigraphy, and geological history of the Noachian basement surrounding the Isidis impact basin, *J. Geophys. Res.* **125**, e2019JE006190 (2020).
(25) M. Attal, J. Lavé, Changes of bedload characteristics along the Marsyandi River (Central Nepal), *Geol. Soc. Am. Spe. Paper* **398** (2006).
(26) G. G., Ori, L. Marinangeli, A. Baliva, Terraces and Gilbert-type deltas in crater lakes in Ismenius Lacus and Memnonia (Mars), *J. Geophys. Res.* **105**, 17629-17641 (2000).
(27) S. Rohais, R. Eschard, F. Guillocheau, Depositional model and stratigraphic architecture of rift climax Gilbert-type fan deltas (Gulf of Corinth, Greece). *Sediment. Geol.* **210**, 132-145 (2008).
(28) F. Salese *et al.*, Estimated minimum life span of the Jezero fluvial delta, Mars, *Astrobiology* **20**, 977-993 (2020).
(29) I.G Hwang, S.K. Chough, "The Miocene Chunbuk Formation, SE Korea: marine Gilbert-type fan-delta system" in A. Colella and D.B. Prior (Editors), Coarse- Grained Deltas. *Int. Assoc. Sedimentol. Spec. Pub.* **10**, 235-254 (1990).
(30) V.R. Baker, D.J. Milton, Erosion by catastrophic floods on Mars and Earth. *Icarus* **33**, 27–41 (1974).
(31) J.E. O'Connor and J.E. Costa, The world's largest floods, past and present (United States Geological Survey circular 1254, 13 pp., 2004).
(32) V.C. Gulick, V.R. Baker, Origin and evolution of valleys on Martian volcanoes. *J. Geophys. Res.* **95**, 14325-14344 (1990)
(33) N. Mangold *et al.*, The origin and timing of fluvial activity at the Eberswalde crater, Mars, *Icarus* **220**, 530-551 (2012).
(34) N. Cabrol and E. Grin, Distribution, classification and ages on Martian impact crater lakes, *Icarus* **142**, 160-172 (1999).
(35) R.M.E. Williams *et al.*, Martian Fluvial Conglomerates at Gale Crater. *Science* **340**, 1068-1072, (2013).
(36) R.E., Milliken, J.P. Grotzinger, B.J. Thompson, Paleoclimate of Mars as captured by the stratigraphic record in Gale Crater, *Geophys. Res. Lett*. **37**, L04201 (2010).
(37) W. Rapin *et al.*, Alternating wet and dry depositional environments recorded in the stratigraphy of Mount Sharp at Gale crater, Mars. *Geology* G48519.1 (2021).
(38) R.E. Summons *et al.*, Preservation of Martian Organic and Environmental Records: Final Report of the Mars Biosignature Working Group. *Astrobiology* **11**, 157-181 (2011).
(39) T. Bosak, K.R. Moore, J. Gong, J.P. Grotzinger, Searching for biosignatures in sedimentary rocks on early Earth and Mars, *Nature Rev. Earth Environ.*. **2,** *490-506* (2021).
(40) J.L. Eigenbrode *et al.* Organic matter preserved in 3-billion-year-old mudstones at Gale crater, Mars. *Science* **360**, 1096-1101 (2018).
(41) A.G. Hayes et al., Pre-Flight Calibration of the Mars 2020 Rover Mastcam Zoom (Mastcam-Z) Multispectral, Stereoscopic Imager. *Space Sci. Rev.* **217**, 29 (2021).

(42) K.M. Kinch, et al. Radiometric Calibration Targets for the Mastcam-Z Camera on the Mars 2020 Rover Mission. *Space Sci. Rev.* **216**, 141 (2020).
(43) A.S. McEwen *et al.*, Mars reconnaissance orbiter's high resolution imaging science experiment (HiRISE). *J. Geophys. Res*. **112**, E05S02 (2007).
(44) M.C. Malin *et al.*, Context Camera Investigation on board the Mars Reconnaissance Orbiter. *J. Geophys. Res.* **112**, E05S04 (2007)
(45) R.L. Kirk *et al.*, Ultrahigh resolution topographic mapping of Mars with MRO HiRISE stereo images: meter-scale slopes of candidate Phoenix landing site. *J. Geophys. Res.* **113**, E00A24 (2008).
(46) R. L. Folk, Petrology of Sedimentary Rocks. Hemphill's (Austin TX), 170pp. (1968)
(47) J. Adams, Sieve size statistics from grain measurements. *J. Geol*. **85**, 209-227 (1977).
(48) M.G. Wolman, A method of sampling coarse riverbed material. *Trans. Am. Geophys. Union* **35**, 951-956 (1954).
(49) J.C. Bathurst, Flow resistance estimation in Mountain Rivers. *J. Hydrol. Eng*. **111**, 625-643 (1985)
(50) A.R. Yingst *et al.*, Morphology and texture of particles along the Spirit rover traverse from sol 450 to sol 745. *J. Geophys. Res*. **113**, E12S41 (2008).
(51) W. Krumbein, L. Sloss, Stratigraphy and Sedimentation. W.H. Freeman and Co., San Francisco, 660 pp. (1963).
(52) K.M. Konsoer *et al.*, Channel slope adjustment in reduced gravity environments and implications for Martian channels. *Geology*, 2018044 (2018).
(53) A.O. Clark, Estimating probable maximum floods in the Upper Santa Ana basin, Southern California, from stream boulder size, Environ. *Eng. Geosci*. **2**, 165-182 (1996).
(54) J. Alexander and M.J. Cooker, Moving boulders in flash floods and estimating flow conditions using boulder in ancient deposits, *Sedimentology*, **63**, 1582-1595 (2016).
(55) M.L Huber, M. Lupker, S.F. Gallen, M.Christi, A.P. Gajurel, Timing of exotic, far-traveled boulder emplacement and paleo-burst flooding in the central Himalayas, *Earth Surf. Dynam*. **8**, 769–787 (2020).
(56) W. Nemec, Deltas: remarks on terminology and classification. In: Colella, A., Prior, D.B. (Eds.), Coarse-Grained Deltas. *Int. Assoc. Sedimentol. Spec. Publ*. **10**, 3–12 (1990).
(57) G. Postma, Depositional architecture and facies of river and fan deltas: a synthesis. In: Colella, A., Prior, D.B. (Eds.) Coarse-Grained Deltas. *Int. Assoc. Sedimentol. Spec. Publ*. **10**, 13-27 (1990).
(58) V. Axelsson, The Lature delta – A study of deltaic morphology and processes. *Geogr. Ann.* **49**, 1-127 (1967)
(59) N. Backert, M. Ford, F. Malartre, Architecture and sedimentology of the Kerinitis Gilbert-type fan delta, Corinth Rift, Greece. *Sedimentology* **57**, 543-586 (2010).
(60) E.S. Kite, J. Sneed, D. P. Mayer, S. A. Wilson, Persistent or repeated surface habitability on Mars during the late Hesperian–Amazonian. *Geophys. Res. Lett*. **44**, 3991-3999 (2017).
(61) J.D. Tarnas *et al.* Orbital identification of hydrated silica in Jezero crater, Mars. *Geophys. Res. Lett.* **46**, 12771–12782 (2019).
(62) A.J. Brown, C.E. Viviano, T.A. Goudge, Olivine-Carbonate Mineralogy of the Jezero Crater Region. *J. Geophys. Res.* **125** e2019JE006011 (2020).
(63) L. Mandon *et al.*, Refining the age, emplacement and alteration scenarios of the olivine-rich unit in the Nili Fossae region, Mars. *Icarus* **336**, 113436 (2020).

(64) C.E. Viviano-Beck *et al.* Revised CRISM Spectral Parameters and Summary Products Based on the Currently Detected Mineral Diversity on Mars. *J. Geophys. Res.* **119**, 1403-1431 (2014).
(65) Y. Zhang, G. Pe-Piper, D. J. W. Piper, Sediment geochemistry as a provenance indicator: Unravelling the cryptic signatures of polycyclic sources, climate change, tectonism and volcanism. *Sedimentology* **61**, 383-410 (2014).
(66) J.F. Mustard *et al.*, Report of the Mars 2020 Science Definition Team. https://mepag.jpl.nasa.gov/reports/MEP/Mars_2020_SDT_Report_Final.pdf (2013).
(67) L.E., Borg *et al.* Science priorities for Mars sample return. *Astrobiology* **8**, 489-535 (2008).
(68) S.M. McLennan *et al.*, Planning for Mars Returned Sample Science: Final report of the MSR End-to-End International Science Analysis Group (E2E-iSAG): A report requested by the Mars Exploration Program Analysis Group (MEPAG). *Astrobiology* **12**, 175-230 (2012).
(69) A. Mittelholz, *et al.* The Mars 2020 candidate landing sites: A magnetic field perspective. *Earth Space Sci.* **5**, 410–424 (2018).
(70) C.S. Borlina *et al.* Re-evaluating the evidence for a Hadean-Eoarchean dynamo, *Science Advances* **6**, eaav9634 (2020).
(71) B. Sutter *et al.*, Evolved gas analyses of sedimentary rocks and eolian sediment in Gale Crater, Mars: Results of the Curiosity rover's sample analysis at Mars instrument from Yellowknife Bay to the Namib Dune. *J. Geophys. Res.* **122**, 2574-2609 (2017).
(72) J. Lewis *et al.*, Pyrolysis of Oxalate, Acetate, and Perchlorate Mixtures and the Implications for Organic Salts on Mars. *J. Geophys. Res.* **126**, e2020JE006803 (2021).
(73) A. Akbulut, S. Kadir, The geology and origin of sepiolite, palygorskite and saponite in Neogene lacustrine sediments of the Serinhisar-Acipayam Basin, Denizli, SW Turkey. *Clays Clay Miner.* **51**, 279-292 (2003).
(74) K. Hickman-Lewis *et al.*, Metallomics in deep time and the influence of ocean chemistry on the metabolic landscapes of Earth's earliest ecosystems. *Scientific Reports* **10**, 4965 (2020).
(75) C. K. Wentworth, Grain size classification. *J. Geol.* **30**, 377-392 (1922).
(76) R. F. Kokaly *et al*., USGS Spectral Library Version 7, U.S. Geol. Survey Data Series 1035, 61 pp (2017).

Acknowledgments: The authors acknowledge the Mars 2020 project's management, engineering and scientific teams for their diligent efforts in making this mission as effective as possible. The authors are grateful to Mars 2020 team members who participated in tactical and strategic science operations. The authors also thank the HiRISE and CRISM instrument teams of the Mars Reconnaissance Orbiter for the use of HiRISE images, the OMEGA instrument team of the Mars Express mission for the use of OMEGA data. NM, OG, GD, CQN, SLM, PP and SM acknowledge the Centre National de Recherches Scientifiques (CNRS) and the Centre National d'Etudes Spatiales (CNES) for the research infrastructures and collaborative networks enabling their participation to rover operations. The authors appreciated helpful suggestions from reviewers. Photographs from Fig. S8A-C were provided by G. Dromart.

Funding :

Centre National d'Etudes Spatiales, France (NM, OG, GD, CQN, SLM, PP, SM)

NASA Mars 2020 Project (JDT, SFS, BH, JFB, KAF, KHW, KMS, RCW, BLE, SMM, RAY, JIN)

NASA Planetary Science Division, Mars Program (JIS)

NASA M2020 Participating Scientist Program under Grant #80NSSC21K0332 (AJW)

NASA Mars 2020 Returned Sample Science Participating Scientist Program (RSSPS) award numbers 80NSSC20K0234 (TB) and 80NSSC20K0238 (BPW)

NASA Post-Doctoral program (JDT)

UK Space Agency Aurora program (SG)

UK Space Agency Aurora Research Fellowship (KHL)

International Postdoc grant from the Swedish Research Council (grant no. 2017-06388) (SHA)

Simons Foundation Collaboration on the Origins of Life, grant #327126 (TB)

Author contributions:

Conceptualization: NM, SG, GD

Methodology - Data processing: OG, PP, SLM, JFB, JIN, MR, AMO, BH, CQN, JDT, RAY, LCK

Project administration: JFB, KAF, KHW, KMS, RCW, SM

Writing – Original draft: NM, SG, GD, AJB, BH, BW, JFB, OG, DLS

Writing – Review & Editing: NM, SG, OG, GD, JDT, SFS, BH, RAY, JFB, OB, TB, BE, KAF, JPG, KHL, SHA, LCK, JMF, SML, JIN, JWR, MR, JIS, DLS, KMS, VZS, AHT, BPW, RCW, AJW, KHW

Visualization: NM, GD, SLM, CQN, BH, JDT, MR, JFB, SFS, FCIII, NRW

Competing interests: We declare no competing interests.

Data and materials availability: Data are available on the Planetary Data System (PDS). Detailed image numbers and links to data of the Perseverance rover SuperCam and Mastcam_Z instruments used in Fig. 1-4, Fig. S2-S4, S6-S7 and Fig. S12 are listed in Tables S1 an S2. Mars Express data of the Observatoire pour la Minéralogie, l'Eau, les Glaces et l'Activité (OMEGA) used in Fig. S11 are available at: https://pds-geosciences.wustl.edu/mex/mex-m-omega-2-edr-flight-v1/mexomg-0001/data/gem04/ and https://pds-geosciences.wustl.edu/mex/mex-m-omega-2-edr-flight-v1/mexomg-0001/data/gem22/.
Mars Reconnaissance Orbiter (MRO) High Resolution Imaging Science Experiment (HiRISE) data used for Fig. 1, Fig. S1, Fig. S9-S11, are available using the following links:
https://hirise-pds.lpl.arizona.edu/PDS/EDR/ESP/ORB_036600_036699/ESP_036618_1985/,
https://hirise-pds.lpl.arizona.edu/PDS/EDR/ESP/ORB_037100_037199/ESP_037119_1985/,
https://hirise-pds.lpl.arizona.edu/PDS/EDR/PSP/ORB_002300_002399/PSP_002387_1985/,
https://hirise-pds.lpl.arizona.edu/PDS/EDR/PSP/ORB_003700_003799/PSP_003798_1985/.
CRISM data used for Fig. S11 are available at: https://pds-geosciences.wustl.edu/mro/mro-m-crism-3-rdr-targeted-v1/mrocr_2101/trdr/2007/2007_029/hrl000040ff/hrl000040ff_07_if183l_trr3.img.
The Context image mosaic of Jezero used in Fig. S1 is available at the United States Geological Survey: https://astrogeology.usgs.gov/search/map/Mars/Mars2020/JEZ_ctx_B_soc_008_orthoMosaic_6m_Eqc_latTs0_lon0. The Entry, Descent, Landing (EDL) image used in Fig. 5 is available on the link https://mars.nasa.gov/mars2020/multimedia/raw-images/.

Supplementary Materials

Materials and Methods

Supplementary Text

Figures S1 to S12

Tables S1 to S3

References (41-76)

Supplementary file "CobblesMeasurements.xlsx"

Figure captions

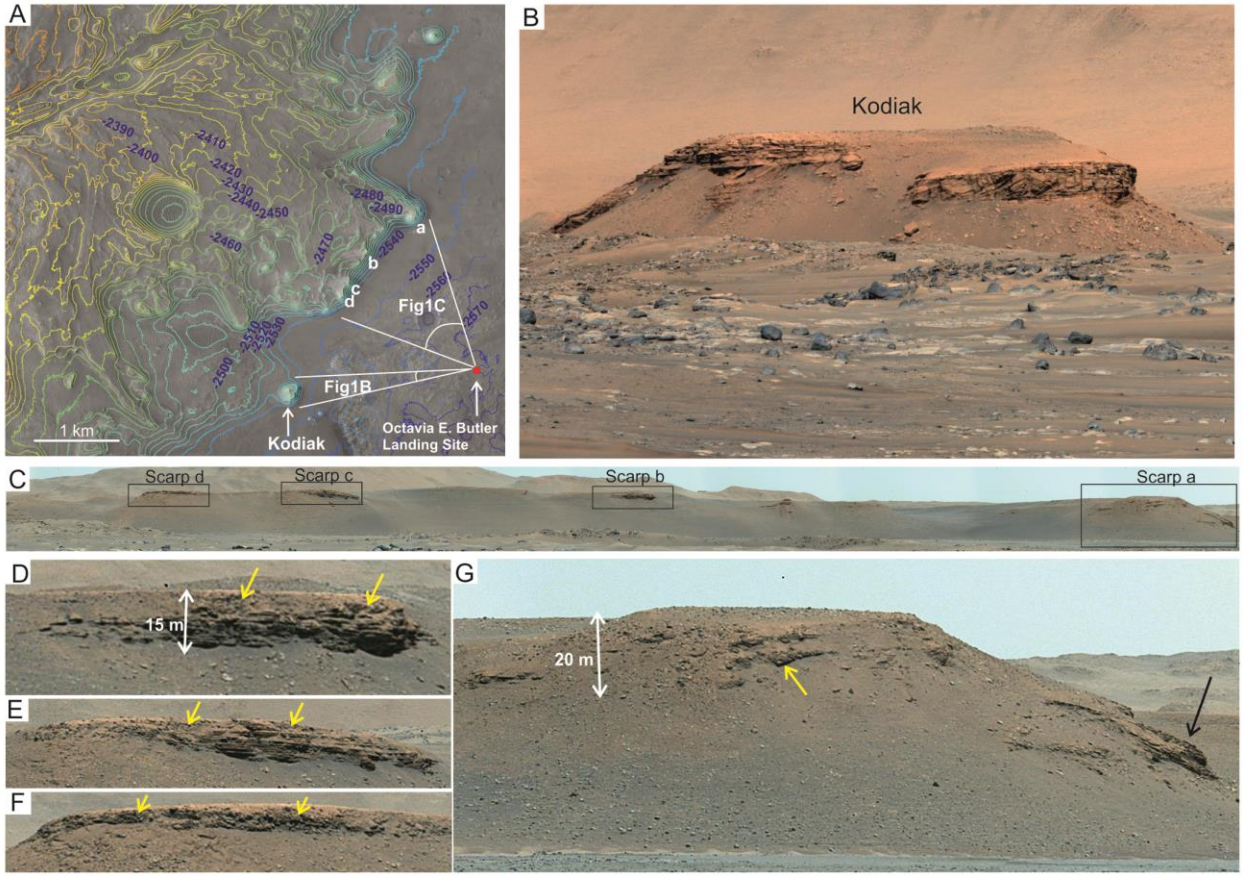

Figure 1: Orbital and rover context observations of the Jezero crater western fan. (A) High Resolution Imaging Science Experiment (HiRISE) mosaic (*14*) with 10 m elevation contours from a digital elevation model (DEM) (*14*) showing the western fan inside Jezero crater and the landing site, informally named the Octavia E. Butler (red dot). White arcs represent the field of view of Fig. 1B and 1C. (B) The butte informally named Kodiak was imaged from a distance of ~2.24 km by Mastcam-Z. (C) Mastcam-Z enhanced color mosaic of the delta front, taken from a ~2.20 km distance with close-ups on scarps of interest (a to d). (D-G) Each scarp is imaged by the corresponding 110 mm focal length Mastcam-Z images. Yellow arrows indicate the location of boulder-rich material shown in Fig. 3-4. The black arrow in (G) indicates an exposure with dipping strata.

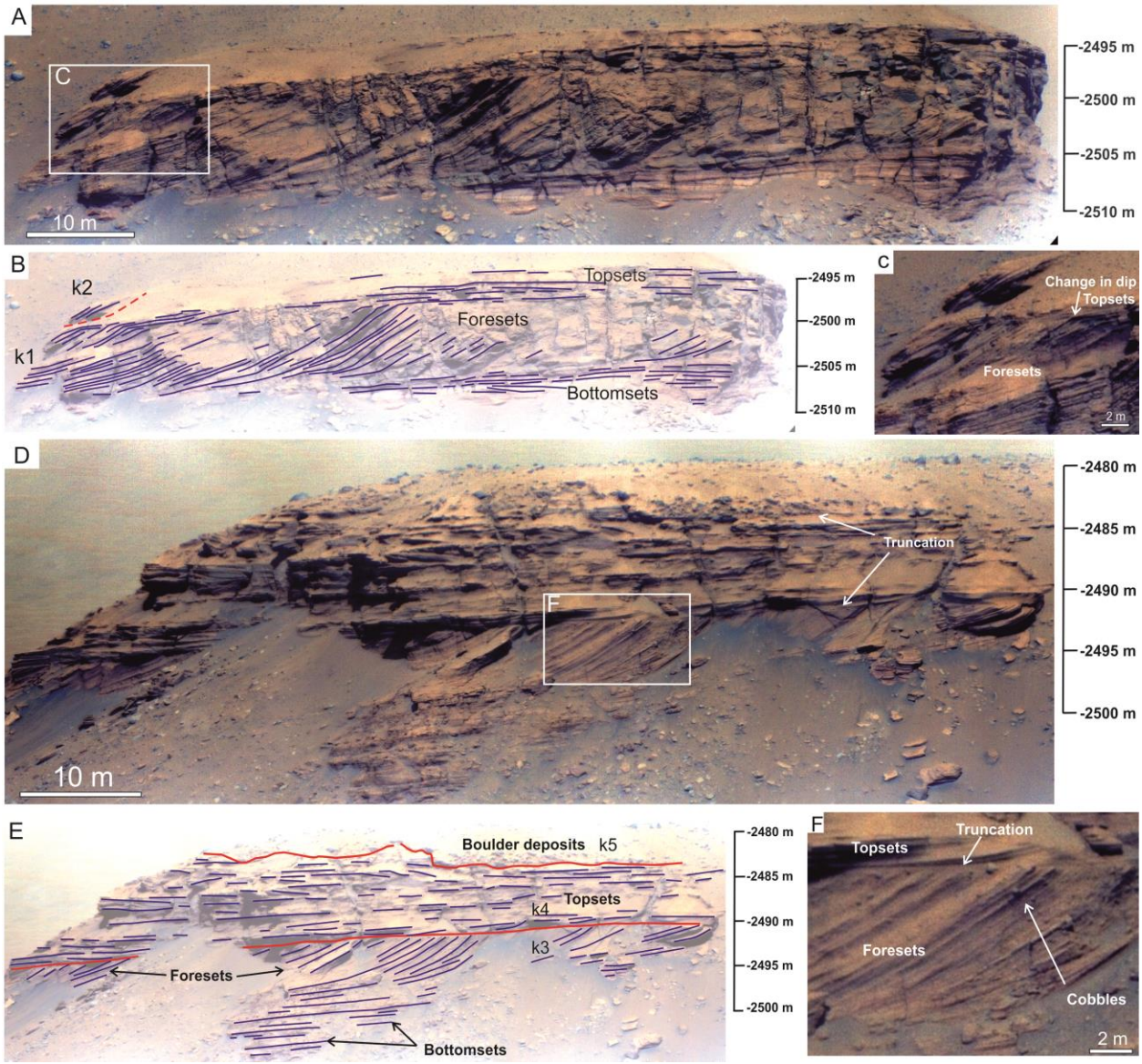

Figure 2: Stratigraphy of Kodiak butte. (A) and (D) Zoomed images of the two scarps of Kodiak (see Fig. S2 for wider context). Elevation scales were inferred from a HiRISE DEM (*14*) and have systematic uncertainties of ±2 m. White boxes indicate regions shown in more detail in other panels. (B) and (E) Interpreted line drawings of the main visible beds (blue lines for individual beds and red lines for discontinuities), overlain on the same images. Units k1 to k5 are labelled, as discussed in the text. (C) Zoomed image of k1 showing the change in dip from sub-horizontal beds (topsets) to inclined beds (foresets). (F) Zoomed image of the foresets in k3. This unit has a coarse texture with several cobble-size clasts (white arrow). The erosional truncation of k3 by k4 is labeled.

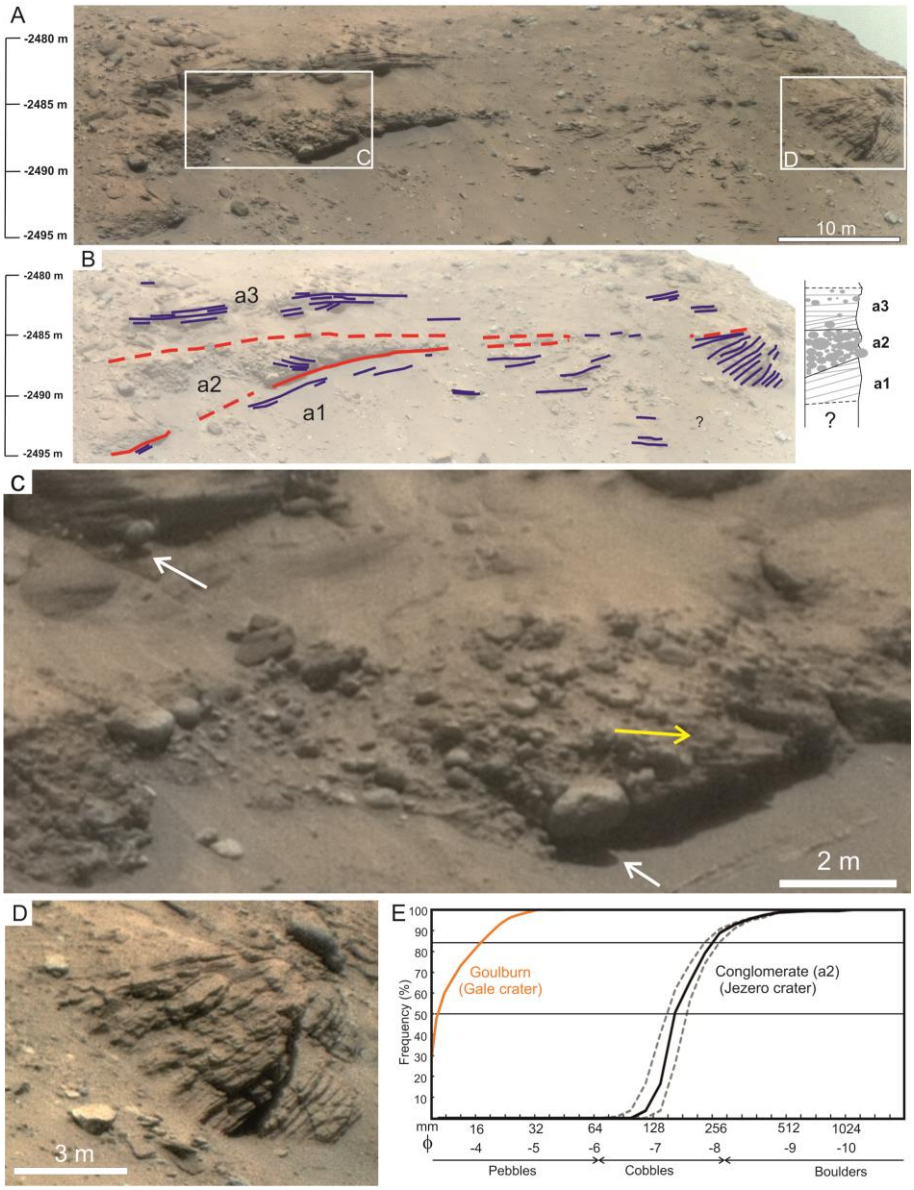

Figure 3: **Stratigraphy of the western fan scarp "a".** (A) RMI mosaic of the western fan scarp "a" (see Fig. S3 for a wider context). Elevation scale as in Fig. 2. White boxes indicate regions shown in more detail in other panels. (B) Interpreted line drawing of individual layers (blue lines) and main boundaries (red lines) between sedimentary bodies labelled a1 to a3. A simplified stratigraphic column of these three bodies is shown on the right. (C) Zoomed image of the boulder-bearing units a2 and a3. White arrows indicate the shadow cast beneath two boulders hanging from the bedrock. Right of the lowermost hanging boulder, an incipient oblique bedding is visible (yellow arrow). Unit a3 might be the result of an amalgamation of two or more depositional sequences. (D). Zoomed images of a1 showing dipping layers organized as co-sets of dipping beds with an apparent dip of up to 30°. (E) Cumulative histogram, on a logarithmic scale (ϕ scale defined by log2 increments), of the measured sizes of 333 clasts (black) compared to the conglomerate Goulburn measured at Gale crater by the Curiosity rover (orange) (*35*). Dotted lines indicate the uncertainty around clast size measurements (*14*).

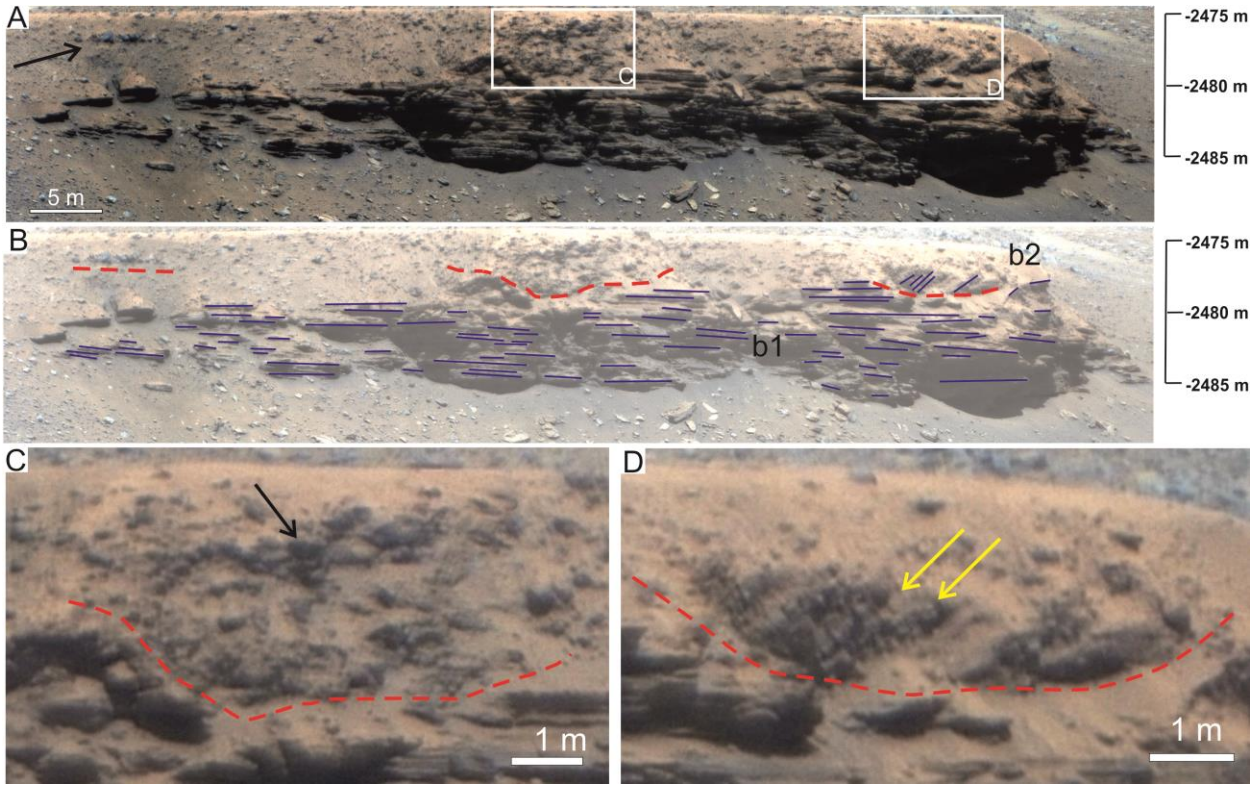

Figure 4: Stratigraphy of the western fan scarp b. (A) Mosaic of five RMI frames of scarp b (localization in Fig. 1, mosaic in Fig. S4). The black arrow at the top left indicates a thin bed with cobbles and boulders preserved in the scarp similar to the thinning of a2 in Fig. 3. Elevations scales are as in Fig. 2. White boxes indicate regions shown in more detail in other panels. (B) Line drawing interpretation of this scarp, showing individual beds (blue lines) and discontinuities (dotted red lines). Sub-horizontal beds dominate the lower sedimentary unit b1. This unit displays a relatively fine-grained material compared to overlying boulder-bearing conglomerates b2, which are present above a discontinuity (dashed red lines) interpreted as a truncation episode. (C) Zoomed image of a boulder conglomerate displaying a series of rounded boulders, piled up along a sub-horizontal bed, 50 cm to 1 m in diameter, developed along a sub-horizontal bed (black arrow). (D) Zoomed image of cobble-bearing conglomerates that were deposited as dipping beds (yellow arrows). The presence of bedding indicates the conglomerate exposure is not a residual lag lying on hillslopes.

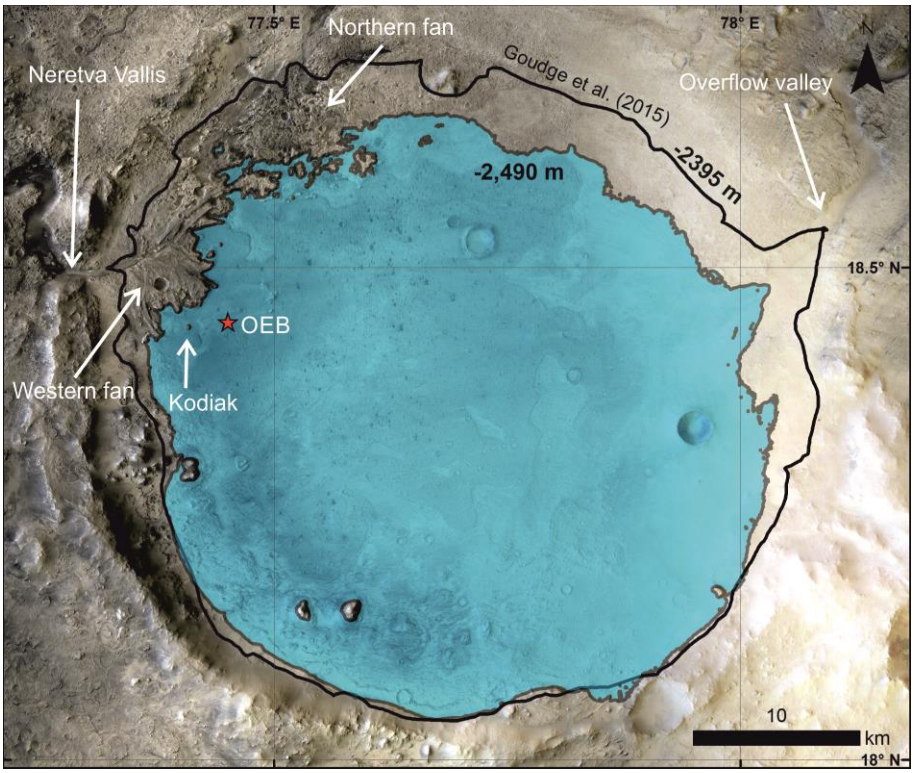

Figure 5: Inferred paleolake level inside Jezero crater at the time of Kodiak sediment deposition. Blue shading indicates assumed lake level filled to the -2490 m gray contour following the uppermost elevation deduced from deltaic architecture at Kodiak (Fig. 2). The red star indicates Octavia E. Butler (OEB) landing site of the Perseverance rover. The black outline of the implied earlier minimum water stand, corresponding to the overflow valley breach (*8*), is shown for comparison. Rocks present on the crater floor might not have been emplaced during the period of lake activity. Both western and northern fans are above the inferred lake surface and the basin appears closed, 100 m below the breach to the east (labeled overflow valley). Background from the Context Camera (CTX) mosaic (*14*).

Supplementary Materials for

Perseverance rover reveals ancient delta-lake system and flood deposits at Jezero crater, Mars

N. Mangold*, S. Gupta, O. Gasnault, G. Dromart, J. D. Tarnas, S. F. Sholes, B. Horgan, C. Quantin-Nataf, A. J. Brown, S. Le Mouélic, R. A. Yingst, J. F. Bell, O. Beyssac, T. Bosak, F. Calef III, B. L. Ehlmann, K. A. Farley, J. P. Grotzinger, K. Hickman-Lewis, S. Holm-Alwmark, L. C. Kah, J. Martinez-Frias, S. M. McLennan, S. Maurice, J. I. Nuñez, A. M. Ollila, P. Pilleri, J. W. Rice Jr, M. Rice, J. I. Simon, D. L. Shuster, K. M. Stack, V. Z. Sun, A. H. Treiman, B. P. Weiss, R. C. Wiens, A. J. Williams, N. R. Williams, K. H. Williford

*Correspondence to: nicolas.mangold@univ-nantes.fr

This PDF file includes:

Materials and Methods

Instruments and dataset

The Mastcam-Z instruments (*11*) are a matched pair of zoomable, focusable, multispectral cameras mounted at a height of ~1.92 m on the Perseverance rover's Remote Sensing Mast (RSM). The fields of view of the cameras range from 26°×19° to 6°×5° degrees from the lowest (26 mm) to highest (110 mm) focal lengths of the zoom system, enabling imaging at pixel scales of ~ 13.5 cm/pixel for features at 2 km distance. The cameras are separated by ~24 cm on the RSM, enabling stereo imaging of features at matched focal lengths (Tab. S1). The RSM can move the cameras over 360° in azimuth and ±90° in elevation, enabling imaging and large-format panoramas to be co-located with data acquired by the Navcam and SuperCam instruments, which are also mounted on the mast. Mastcam-Z can acquire images using standard red, green and blue (RGB) filters, as well as through a set of 11 narrowband filters spanning a wavelength range of 442 to 1022 nm (*11*). To accentuate color variations, the RGB channels can be adjusted for "enhanced color" products, which include more blue and green hues than the human eye would see on Mars (e.g., some rocks and the sky are blue). Mastcam-Z images are calibrated to radiance units using the coefficients derived from the instrument's radiometric calibration (*41*) and converted to radiance factor (*I/F*) units using near-simultaneous images of the Mastcam-Z calibration target (*42*). Mastcam-Z spectra of features within an image are extracted by manually selecting common regions of interest (ROIs) from right and left camera images and averaging *I/F* values of ROI pixels. Right and left camera filters are scaled to average values at 800 nm (the R1 and L1 filters). Error bars shown in Mastcam-Z spectra represent the variance of pixels within the ROI, not instrumental noise, which is lower; filter-to-filter accuracy is <5% (*41*). Narrowband filters enable limited mineralogical information to be inferred from the acquired images, sensitive to iron oxides, oxyhydroxides, and/or oxyhydroxysulfates as well as iron-bearing silicates.

SuperCam's Remote Micro-Imager (RMI) provides high-resolution color images (*12*, *13*). SuperCam's RMI is a 2048×2048 pixel camera, with Bayer color filters, mounted on a 110 mm diameter Schmidt-Cassegrain telescope with a focal length of 563 mm. The angular size of the RMI pixels is 10.1 μrad, with a spread function over several pixels. This corresponds to approximatively 2.2 cm pixel^{-1} at a distance of 2.2 km (Tab. S2). The effective resolution (i.e., the capacity to distinguish individual objects) varies depending on image quality and illumination from 4 to 8 pixels, the latter being defined as a minimum contrast of 20% on a calibration target known as US Air Force 1951 Test. The main correction applied to these images is a division by a reference flat field acquired before takeoff to compensate for the vignetting of the instrument. RMI images are assembled in mosaics using a fusion algorithm weighted by the angular distance to the center of each image. A final deconvolution step based on a Lucy-Richardson algorithm has been used to increase sharpness. Figures 2 to 4 are close-ups from within these three mosaics.

Orbital images used for the Digital Elevation Model (DEM) are High Resolution Imaging Science Experiment (HiRISE) images (*43*) from Mars Reconnaissance Orbiter (MRO) with pairs of image numbers ESP_036618_1985 and ESP_037119_1985, ESP_042315_1985 and ESP_037396_1985, PSP_002387_1985 and PSP_003798_1985. Mosaics were assembled in a Geographic Information System. DEMs were constructed using HiRISE stereo image pairs and the ConTeXt Camera (CTX) of MRO stereo image pairs (*44*). The HiRISE DEMs have been computed by stereo-photogrammetry using the SOCET-SET software (*45*) at a spatial resolution of 1 m pixel^{-1}.

Measurement of clast size and shape in boulder conglomerates

Cobbles and boulders in conglomerate a2 were measured using a spatial sampling of 2.2 cm per pixel on the RMI images (Fig. 3, Fig. S6-S7). The long axis and short axis were measured and the diameter of each clast was obtained by averaging these two values. The quality and resolution of the image enables identification of objects as small as 4 pixels across. We chose to measure objects >4 pixels along the short axis, thus measuring clasts ≥ 11 cm (5 pixels), and defined an uncertainty of ±1 pixel for each measurement made. From the distribution of clast sizes, we determined percentile values for clast size, D_n, where n refers to the percentage of clasts smaller than n. The two most commonly used grain size distribution parameters in sedimentary studies correspond to the median clast size (D_{50}) and the size at which 84% of the clasts are smaller (D_{84}), both being used for discharge rates estimations. We obtained a D_{50} of 17.6±2.2 cm and a D_{84} of 27.5±2.2 cm. Nonetheless, the resolution of the image inherently leads to an underestimation of the number of clasts with sizes smaller than 11 cm. In some locations clasts were visible but not measurable due to unclear edges, superimposition of clasts, etc. In areas where the resolution enables a complete measurement, we estimate that ~70 to 80% of the area analyzed is occupied by measured clasts, thereby limiting this overestimation bias. Note that the remaining area does not mean it is only composed of smaller clasts, because some large clasts could be partly hidden by others. Nevertheless it allows us to estimate the bias by assuming that 30% of clasts are smaller

than resolution, such as in the bins <1 cm as an extreme case. This leads to D_{50} values lowered by only 1.2 cm and D_{84} values lowered by 1.6 cm. This bias is added to the previous values, such that D_{50}=16.4±2.2 cm and D_{84}=25.9±2.2 cm.

Clast size analysis discussed here is 2D, and differs from that often carried out for clastic sedimentary rocks on Earth, where grain-sizes may be separated by sieves and/or other devices and quantified and interpreted on the basis of mass distributions (e.g., *46*). Instead, our data are grain counts and thus cannot be directly compared (e.g., *47*). The approach used here is more analogous to the "Wolman pebble count" technique (*48*) that has been used for evaluating flow discharge rates according to the Darcy-Weisbach equations (*49*). Such an approach has also been applied to conglomerates using images acquired at Gale crater (*35*), although those conglomerates were imaged at much closer distances (<5 m).

Another parameter of interest is the shape factor, corresponding to the long axis/short axis ratio. This ratio is 0.545±0.035 on average for the 333 measured cobbles and boulders. As the limit of resolution may affect the statistical meaning of this ratio, we also measured the corresponding values for boulders only (i.e., >25 cm clasts): The calculated ratio for boulders is 0.558±0.039, not substantially different from the value for the entire population. This shape ratio suggests limited elongation and a lack of internal rock fabric at sub-meter scales, e.g., no fine layering, no schistosity, etc.

To assess clast roundness, we employed a method designed to provide estimates of clast roundness (essentially a measure of the sharpness of a clast's corners and edges) using two-dimensional images acquired remotely (*50*). The primary constraint affecting assessments of roundness in this case is image resolution, which in practice means that corners and edges must be resolved over at least 5 pixels, corresponding to ~100 pixels along the long axis to assess angular clasts (*50*); this requires a far finer resolution than is available. However, this constraint assumes that clasts will be binned into all categories commonly used in these assessments, e.g., very angular, angular, sub-angular, sub-rounded, rounded and well-rounded (*51*). To assess whether some level of rounding has occurred allows a much coarser resolution to be used, because it requires only that the overall curve of a corner or edge be resolvable. Here we used a minimum of 15 pixels in average size as the threshold for clasts to be included in the roundness assessment. Additionally, we examined only clasts that were in focus, and for which an entire two-dimensional profile was visible; clasts were not included in our analyses if they were partially draped by unconsolidated material or had outlines that were otherwise obscured (e.g., by shadowing or other clasts). Clasts were assessed qualitatively using roundness chart (*51*). This chart was chosen over other common charts as it shows outlines only, thus lessening the risk of conflating texture with shape. A total of 24 clasts met the criteria noted; of which 13 were assessed as having evidence of modification resulting in rounding and 11 were assessed as essentially angular (little to no rounding). Thus, 54% of clasts resolvable at this distance were found to be substantially rounded.

Discharge rate estimations

The Darcy-Weisbach equations are usually applied to estimations of discharge rates (hereafter Q) (*20, 21*), where estimations of channel width W, water height H, and slope s can be made in association with measurements of clast size distribution (e.g., *49*). This relation has been modified for Mars conditions enabling the use of local Martian gravity g_m (3.72 m s^{-2}):

$$Q=A(8g_mRs/f)^{1/2} \quad \text{(S1)}$$

in which A is the cross-sectional area ($A=W.H$ assuming a rectangular shape), R is the hydraulic radius (the ratio of the cross-sectional area A to the wetted perimeter P, with $P=2H+W$). The parameter f is an empirical factor initially related to the roughness of the channel base. A number of field and laboratory studies have provided values for the friction factor f as a function of the nature of the channel bed and flow conditions (*20, 21*):

$(8/f)^{1/2}=2.2(R/D_{50})^{-0.055}s^{-0.275}$, for gravel beds. (S2)
$(8/f)^{1/2}=8.46\log10(R/D_{50})^{0.1005}$, for a sand bed. (S3)
$(8/f)^{1/2}=5.75\log10(R/D_{84})+3.514$, for a gravel bed. (S4)
$(8/f)^{1/2}=5.62\log10(R/D_{84})+4$, for a boulder bed. (S5)

At fixed parameters, Equation (S2) gives the lowest estimates and (S5) the highest estimates of the friction factor *f*, and these values are used in Tab. 3. Equation (S5) deduced from boulder beds is also in agreement with the presence of boulders in unit a2. D_{50} and D_{84} are taken from the clast size distribution (see previous section) in order to place a lower bound or upper bound respectively, yielding D_{50}=0.142 m and D_{84}=0.281.

Assumptions made for the channel size are first-order constrains. Firstly, we assume that the shape of a2 corresponds more or less to half a channel (partly covered by scree on the other half) leading to a channel around 50 m wide. To account for uncertainty, we include a minimum channel width of 30 m and a maximum of 100 m. Secondly, channel depths follow the empirical rule $H=0.164W^{0.66}$ for bankfull flows in Earth rivers, a scaling law that is assumed not to differ substantially on Mars despite the lower gravity (*52*). Values deduced from that law suggest depths of 1.55 to 3.4 m for 30 and 100 m channels, respectively (Tab. S3). These values correspond to the minimum expectations in the case of a 30 m channel. Given that the flow is of flood type, the scaling ratio may underestimate the actual channel height. As such, we also include an estimation of channel *H* from the apparent thickness of 7 m of the unit a2, using the 50 m width as a reference.

To calculate the slope, we used values determined from the base of the channel deposits (see next section). The slope at the base of conglomerate a2 is 0.014, but this value is constrained by only two points. This slope is close to that measured at the top of the plateau (*s*=0.012). The basal slope estimated at scarps b to d reaches 0.029 (see supplementary text), so the basal slope of a2 could be underestimated. Consequently, we use conservative values, 0.012 and 0.029, respectively, for the minimum and maximum estimates.

Another approach to estimate velocities and discharge rates is based on the largest clast lifted up by the flow. Such a method has been used on Earth from empirical datasets (*18*) not taking into account gravity. Several studies have developed methods taking into account gravity (*53*-*55*) by estimating the critical force necessary to initiate the motion of boulder (*53*):

$$V = 1.2\sqrt{\frac{2}{C_L+C_D}} * \left\{\frac{\rho r\left(\frac{\pi}{6}*D3\right)*\frac{\rho r-\rho f}{\rho f}*g*(\cos(s)*\mu-\sin(s))}{(D/2)^2*\pi}\right\} \quad \text{(S6)}$$

This method was refined by defining the net force derived as the sum of drag-force and frictional forces subtracted by impulsive force, giving the following velocity (*54*):

V= (4/3 $Dg(p_r/p_f$-1)μ-0.5a/g)$^{0.5}$ for a spherical clast (S7)

Both approaches require the knowledge of the density of the fluid and of the rock. We fix those to be ρ_f=1100 kg m^{-3} for the fluid (a value typical of moderately debris-laden aqueous flows, *19*) and ρ_r=2900 kg m^{-3} (a value typical of mafic block of crust), as well as the diameter of the block *D* taken as 1.25 m as observed in unit a2. Both equations include the gravity *g*, and the first one requires knowing the local slope *s* that we fix from our two end-member values of 0.012 and 0.029. C_L and C_D are lift coefficient and drag coefficients, respectively, which are taken as in the original study for a spherical shape (*53*). Lastly, the parameter *a* is the acceleration fixed at 0.5 m s^{-2} as defined in (*54*). We used existing software codes for these calculations (*55*).

These calculations have only been done for the unit a2 for which we have estimated the clast size and their distribution. Other boulder conglomerates b1 and k5 display much more scree on the slope, and thus do not enable us a measurement of the clast size distribution. However, an estimation of the largest clast can be done, and those are 1 to 1.3 m in these units. As they are of similar size as in a2, the threshold velocity measured from the largest clast size would be of the same magnitude.

Table S3 summarizes discharge rate estimations using Equation (S1) coupled with Equation (S2) for the lower limits and Equation (S5) for the upper limits. These estimates vary from 1.63 to 8.64 m s^{-1} for velocities and 76 m^3 s^{-1} to ~3000 m^3 s^{-1} for discharge rates. Results using Equations (S6) and (S7) show that the threshold velocity to lift up a 1.25 m diameter block varies from 1.91 to 2.97 m s^{-1}, and the corresponding discharge rates would range from 88 to

1011 $m^3 s^{-1}$, thus within the range obtained by previous methods (Equations S1-S5). These values are classical discharge rates similar to that of flood flows in mountain rivers (from various origins) and are two orders of magnitude lower than megafloods such as Icelandic jökulhaups (subglacial volcanoes) and Washington State's Channeled Scablands (ice-dam failure), which are from 10^5 to 10^7 $m^3 s^{-1}$ (*30, 31*).

Supplementary Text

Gilbert deltas on Earth

A delta is defined as a sedimentary deposit built by a fluvial feeder system flowing into a standing body of water. Sedimentological studies of ancient deltas on Earth recognized a tripartite geometrical association comprising topsets, foresets and bottomsets (Fig. S8). In the upper division of a Gilbert-delta, topsets are fluvial strata formed along lines of deposition parallel to the upper surface of the delta. In the middle division, foresets are steeply inclined beds forming parallel to the delta front. In the lower division, bottomsets are gently inclined strata forming at the downdip termination of foresets.

Gilbert-type deltas are characterized by a series of related criteria: (i) a dominantly coarse-grained deposit (i.e., sands and gravels) topset fluvial beds that dip gently basinward (0–5°); (ii) steep subaqueous depositional delta front slopes, dipping typically 10–40°; (iii) gently inclined (<10°) bottomset beds that taper basinward and are commonly fine-grained. Gilbert-type deltas are part of the broad family of steep-face, or coarse-grained, deltas (*56*). Earth's Gilbert-type deltas are linked to a variety of distributary fluvial systems, including very steep topographic gradient enhanced by ephemeral fluvial discharges in fault block, mountain front, fjord margin, volcanic highland settings, and fluvio-glacial outwash, steep gradient braided river plains settings (*57*).

The conditions to form a steeply inclined Gilbert-type profile, across which slipface processes dominate, are (*58*): (i) sufficiently large water depths immediately adjacent to the fluvial mouth to provide space for sedimentary deposition; (ii) transport of bedload as far as the fluvial feeder mouth; and (iii) expansion of the fluvial effluent as an axial turbulent jet (inertia-dominated effluent diffusion). Corresponding water depth can vary from ~20 m (Fig. S8) to ~900 m on Earth (e.g., Gulf of Corinth, Greece) (*27, 59*). The fluvial bedload/total-load ratio must be high, and the mud fraction low, such that the front of the delta progrades faster than the lower part of the delta slope, resulting in the oversteepening of the delta front. Gilbert-type deltas preferentially develop in low-energy basins, with limited wave and tide influence (*56*), because their axial inertia-dominated fluvial diffusion is not disturbed.

The Kodiak butte displays the architecture indicative of Gilbert-deltas. The elevation of the topset-foreset transition gives the elevation of the lake level at the time of deposition. The SW delta front does not provide similar clean scarp faces as observed at Kodiak, but does contain possible topset strata such as unit b1. Fine sediments (e.g. mudstones) are expected to weather easily into unconsolidated scree, so the scarcity of clean faces could be due to erosion, perhaps explaining why the whole set of layers cannot be observed there.

Analysis of the delta front from orbital data

Observations of the residual lag above units a3, b2 and k5 enable us to link the coarse deposits with materials identified in orbital imagery (Fig. S9). The presence of well-rounded, massive, meter-scale boulders similar to those observed within the immediately underlying a2, b2 and k5 units suggests the presence of flood deposits that were weathered out by erosion. The residual lag includes rocks weathered out from both types of sedimentary bodies: fined-grained rocks such as sandstones and boulder conglomerates (Fig. S9). From orbital data, this residual lag was mapped as the Delta Blocky unit and interpreted as fluvial channel deposits (*15, 23*). This interpretation is consistent with our rover observations.

The Delta Blocky Unit overlies other delta fan deposits such as the Truncated Curvilinear Layered Unit deposits that represent finer-grained material (Fig. S1, *15, 23*). Identification of several contacts at the base of the blocky deposits enables us to estimate the slope on which these deposits formed (between 0.009 and 0.033) (Fig. S10). Measurement points (Fig. S10) are those for which a unconformable contact has been observed between the Delta Blocky Unit and the underlying units (e.g., the Delta Truncated Curvilinear Layered Unit in the proximal and middle fan sections, and

the Delta Thickly Layered and Delta Thinly Layered units in the distal fan section) (the top elevations of the Delta Blocky Unit were not considered because of the potential late erosion, conducive to the modification of the original depositional profiles). A total of 37 observation points were identified. These locations were then projected onto a number of radiating cross-lines from the avulsion nodes to build the lower depositional profiles of the Blocky Unit. Profiles of the central Blocky Unit (profiles w1, k and bcd) appear fairly constant, varying between 0.026 and 0.029. Northern profiles (n2 and a) show more gentle gradients of 0.014. Slope breaks may be expressed in profiles n1 and n2 (Fig. S10). The current thickness of the Blocky Unit ranges from 2 to 26 m, which represent a minimum depositional thickness given subsequent erosion.

Results also show that the base of the deposits was a continuous surface. We have searched for buried impact craters along this contact to evaluate whether a hiatus of deposition occurred before channel formation, as was previously conducted on Martian alluvial fans (*60*). The lack of buried craters points towards a continuity in deposition, although small craters could be invisible due to preservation issues. As such, the lack of buried craters suggests either continuity in deposition or a limited depositional hiatus (for instance, >10 Myrs would enable a large number of small craters to form).

Sources of sediments

Compact Reconnaissance Imaging Spectrometer for Mars (CRISM) and Observatoire pour la Minéralogie, l'Eau, les Glaces et l'Activité (OMEGA) data of the Neretva Vallis basin and of Jezero crater western delta fan were analyzed to provide information on the source(s) of the material in the delta. The color composite of the OMEGA map (Fig. S11A) shows olivine, LCP (low-calcium pyroxene) and HCP (high-calcium pyroxene) spectral parameters indicating the predominance of pyroxene (dominated by LCP) in the watershed of Neretva Valles (dark line) and within Jezero crater rim. The olivine-bearing material in purple dominates 60 km downstream of Neretva Valles before its entrance to Jezero crater. This olivine spectral signal corresponds to the regional olivine-bearing unit (*59*). Thus, the Neretva Vallis basin includes multiple lithological units, the far reaches of which are dominated by LCP and Fe/Mg smectite-bearing crust, the portions ~10-60 km away are dominated by olivine ± carbonates (also present near the landing site), and the nearest portions incise Jezero rim LCP-bearing rocks without appreciable hydration (*7*, *24*) (Fig. S11).

The mineralogy of the Jezero delta system has been determined to be both mafic and hydrated, containing olivine and low-calcium pyroxene (LCP), Fe/Mg-smectite, carbonate and local exposures of hydrated silica or Al-clays based on orbital observations (*6-7, 61-64*). CRISM analyses of the delta front exposures imaged by the RMI show LCP- and phyllosilicate-bearing endmembers (Fig. S11). The blocky unit capping the delta and interpreted as fluvial channel deposits appears to contain LCP without a strong contribution from hydrated minerals. In addition, Mastcam-Z multispectral observations of the delta scarp show that the conglomerate unit and delta front talus exhibit visible and near-infrared (VNIR) spectra that are similar to LCP-bearing Noachian basement exposed in the Jezero crater rim (Fig. S12). In both locations, Mastcam-Z observations show a broad absorption near 900 nm consistent with LCP observed in these areas using CRISM. However, the thinly layered outcrop is more variable. Although some areas in the thinly layered unit also show similar LCP-like signatures, other areas exhibit signatures consistent with minerals like olivine instead.

It is difficult to determine the source of sediments on the basis of surface exposure maps alone because sources may be eroded, buried or otherwise obscured (e.g., *65*). Nevertheless, clast size distribution and rounding in the observed Jezero sediments, though not definitive, are consistent with substantial transport. For example, pebble distributions along rivers in the Himalaya shows crystalline pebbles transported between 50 and 200 km with *D50* sizes of 10–20 cm (*25*), similar to the distribution obtained for the a2 unit. The rounding characteristics and massive shapes of boulders are also consistent with igneous source rocks rather than the less-resistant olivine-unit (*63*). The average ratio of long axis to short axis of 0.558±0.039 for boulders suggests a lack of sub-meter scale rock fabric as might be expected for sedimentary rocks. Thus, grain size distributions and grain characteristics suggest that a substantial fraction of the rocks could be transported from distances of >60 km upstream of Jezero crater, where widespread exposures of LCP-rich crust have been identified. Closer sources, such as Jezero's rim, which is also enriched in LCP, would also have contributed, possibly explaining the angular boulders. In summary, our observations suggest a source of the LCP-bearing blocky deposits within the LCP-bearing crust that is exposed along the rim of Jezero crater, within the crust >60 km upstream, or both.

Importance for sample collection

The Mars 2020 mission is designed to collect samples for return to Earth (*66, 67*). The boulders observed in the deltaic sedimentary rocks of Jezero crater enable multiple synergistic investigations to be conducted on the same rock, such as geochronology, geochemistry, petrography, and paleomagnetism (*4*). Due to the large range in clast sizes (up to 1.5 m) observed in the delta front, there may be an opportunity to collect sample cores from individual boulders (either angular or rounded, from various transport distances) as well as mixtures of smaller (D <1 cm), diverse, detrital grains from this sequence of ancient Martian sedimentary rocks. Either case could provide important constraints on the regional geological history prior to the deposition of the Jezero delta (*4, 67-69*).

Our observations of the Kodiak remnant are consistent with the interpretation of the sediment fan below the conglomerate deposit in Jezero crater as a delta potentially containing mudstones. Mudstones in Gale crater preserve indigenous organic compounds that appear to be predominantly macromolecular (*40, 71*). These compounds may be of Martian or exogenous origin, abiotic, prebiotic or biologically derived (*39*) and additionally modified by oxidation at the Martian surface (*72*). The macromolecular nature and low abundance of this material, as well as the abundance of oxychlorine species, complicate *in situ* analyses (*69*). Known to preserve organic compounds in ultramafic terrains on Earth (*73*), Fe/Mg smectite has been detected by CRISM in Jezero delta and various delta remnants, including the Kodiak delta remnant (*10*) and we therefore predict it occurs in mudstones in the bottomset beds at Kodiak (Fig. 2). Mudstones on Earth dating to 3.3-3.0 Ga exceptionally preserve organic materials with geochemical characteristics suggesting biogenic origins (*74*).

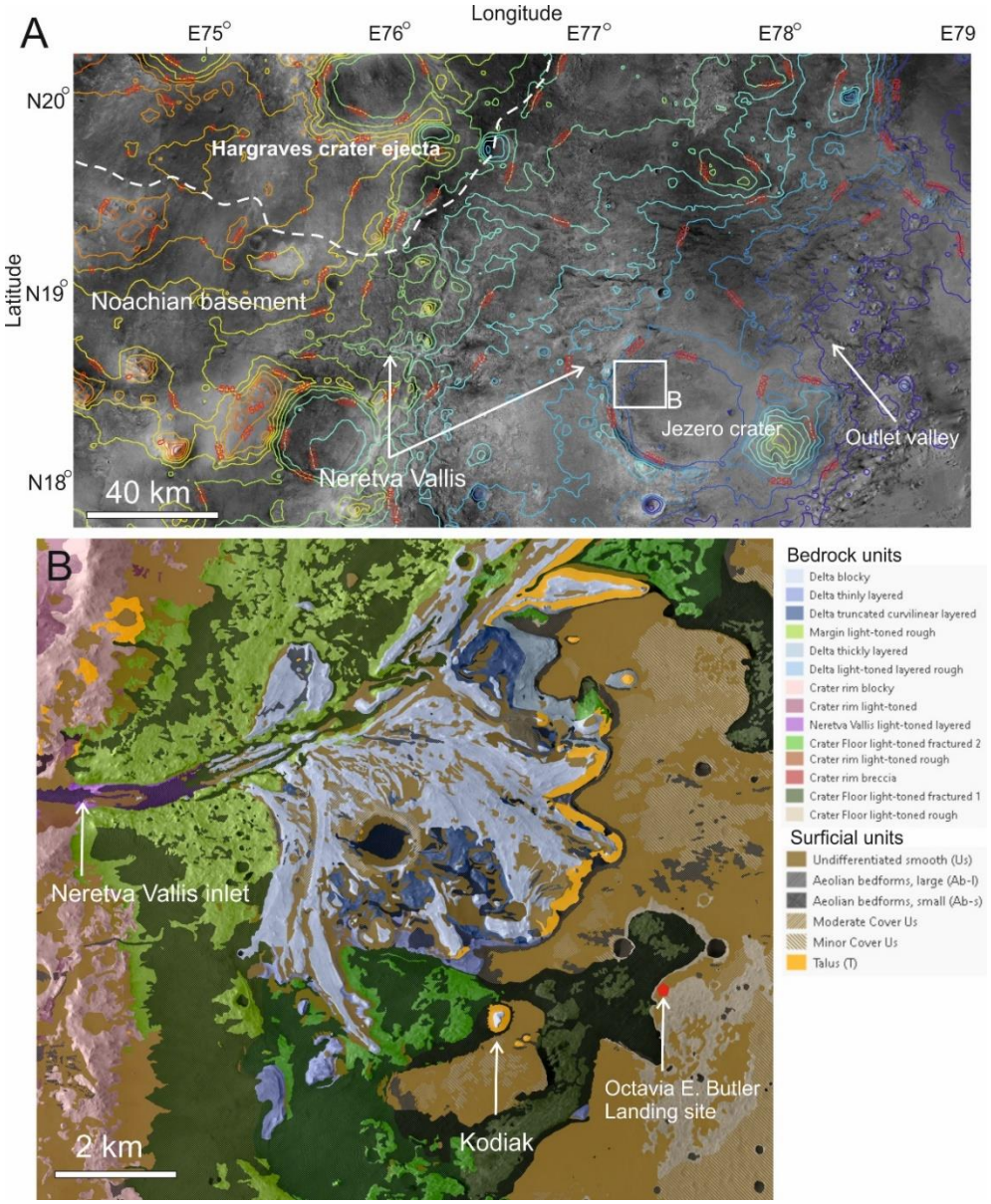

Figure S1: Geologic context of the Jezero crater delta. (A) CTX mosaic (*14*) with Mars Observer Laser Altimeter altimetry showed as contours. Jezero crater lies in the eastern part of the Nili Fossae region. The western fan was formed from the deposition of sediment transported through Neretva Vallis, a 200 km long fluvial valley incising the Noachian basement west of Jezero crater. Jezero crater displays an eastern breach with an outlet valley also visible in topographic data. (B) Geologic map of the Jezero western fan (*15*). The Delta Blocky Unit (light blue, devoid of apparent layering) caps the western fan and superimposes the Delta Truncated Curvilinear Layered Unit and the Delta Thinly Layered Unit. The Perseverance rover landed at the Octavia E. Butler landing site (red dot), 2 km from the delta front. The delta front visible from the rover features many large talus deposits dominated by scree (orange color on the geological map). The Kodiak butte is located at the southern edge of the delta.

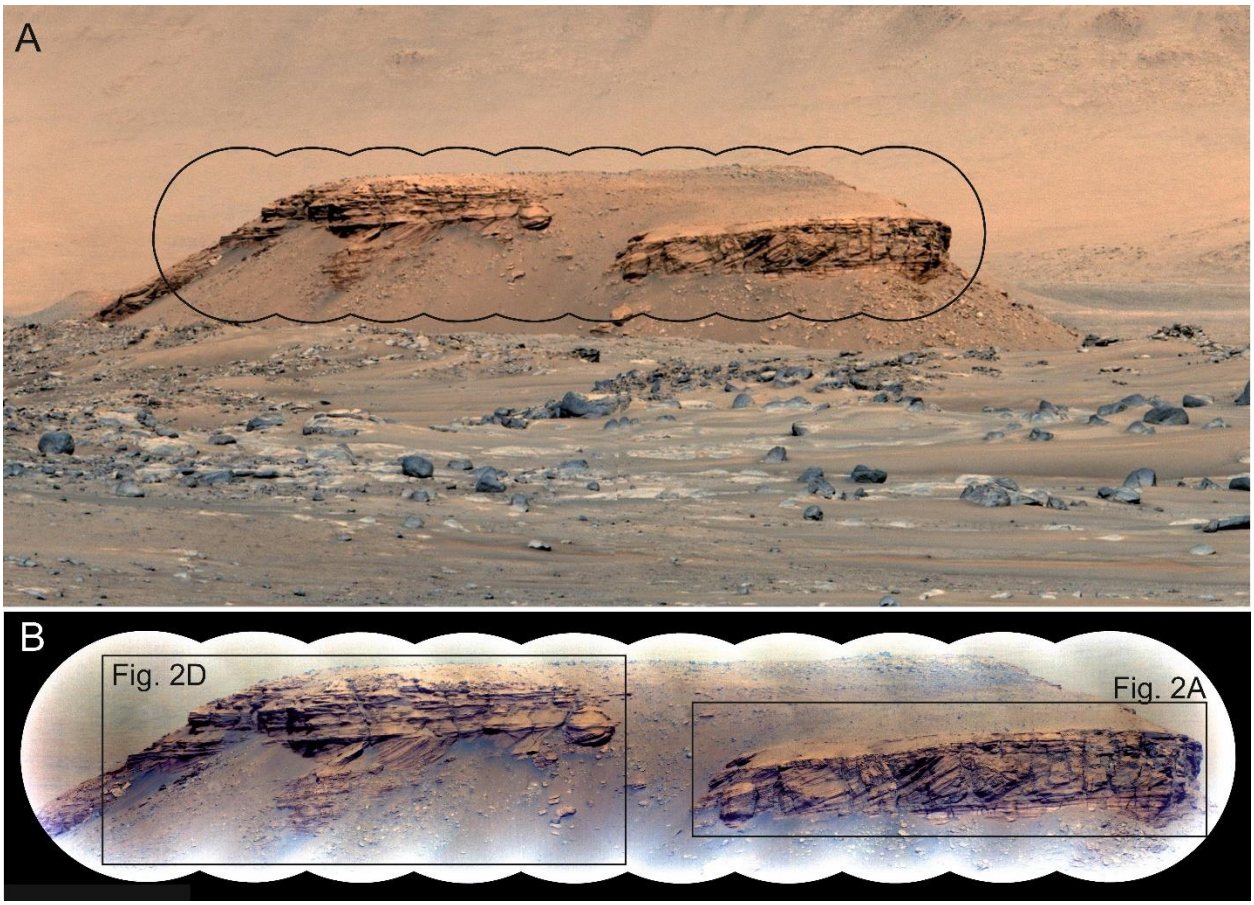

1030

Figure S2: Images of Kodiak. (A) Mastcam-Z right camera enhanced color stretch image of Kodiak butte (see Fig. 1) with footprints of the SuperCam RMI mosaic. (B) SuperCam RMI mosaic with enhanced color stretch. See Tab. S1 and S2 for more details.

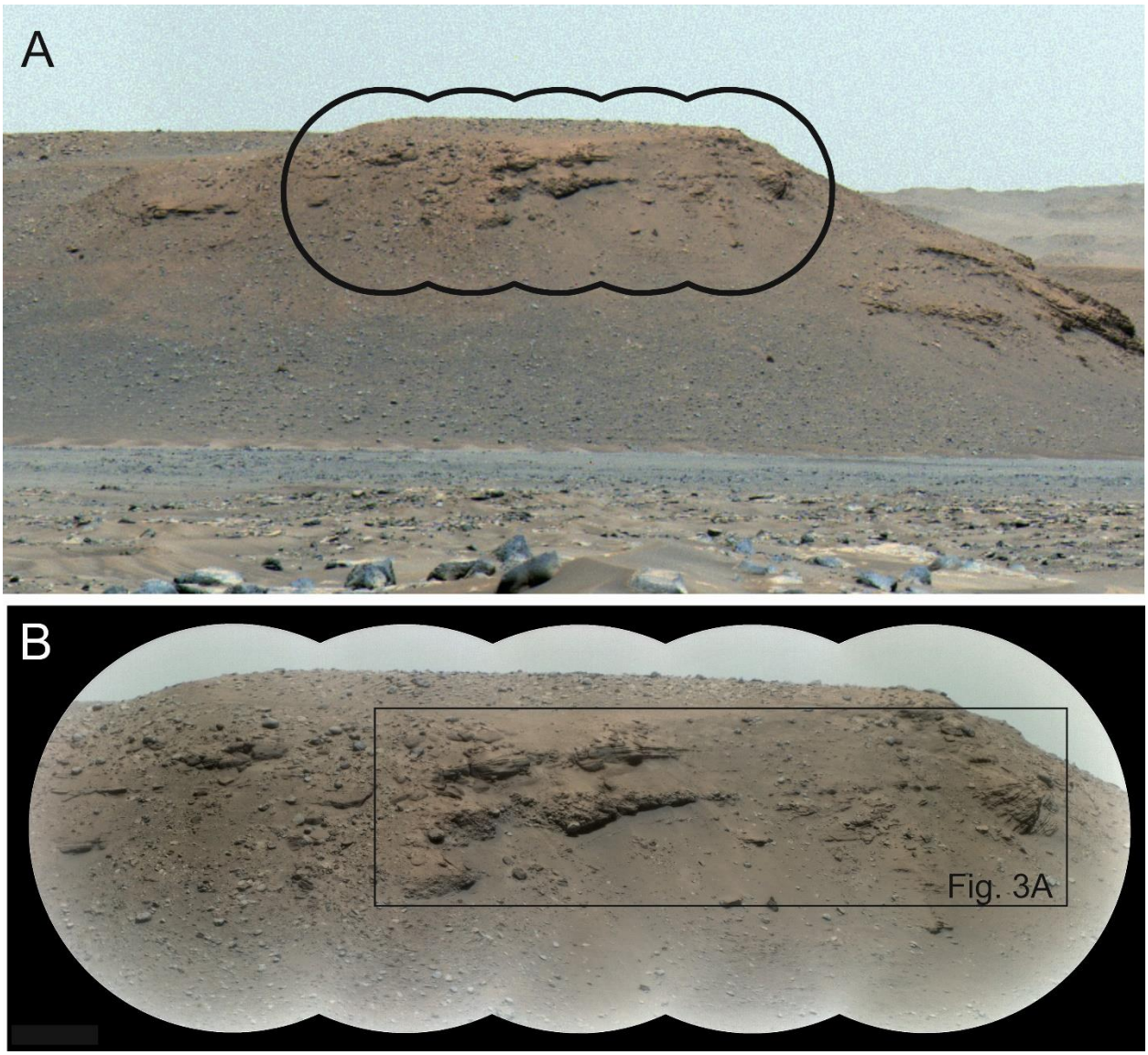

Figure S3: Images of the delta front, scarp "a". (A) Mastcam-Z left-camera enhanced color stretch image of delta front scarp "a" (see Fig. 1) with footprints of the SuperCam RMI mosaic. (B) SuperCam RMI mosaic with enhanced color stretch. See Tab. S1 and S2 for more details.

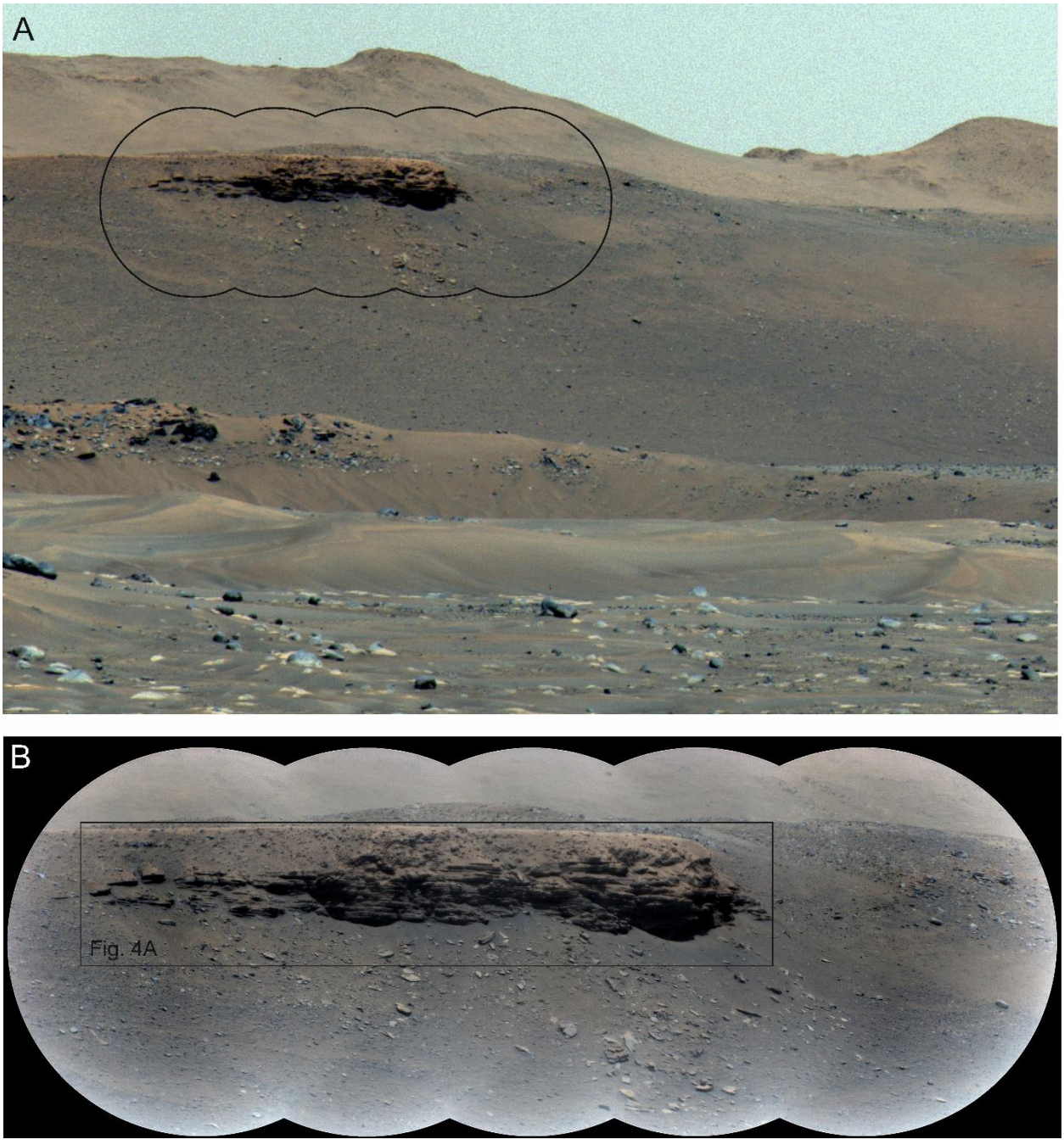

Figure S4: Images of the delta front, scarp b. (A) Mastcam-Z left-camera enhanced color stretch image of delta front scarp b (see Fig. 1) with footprints of the SuperCam RMI mosaic. (B) SuperCam RMI mosaic with enhanced stretch color. See Tab. S1 and S2 for more details.

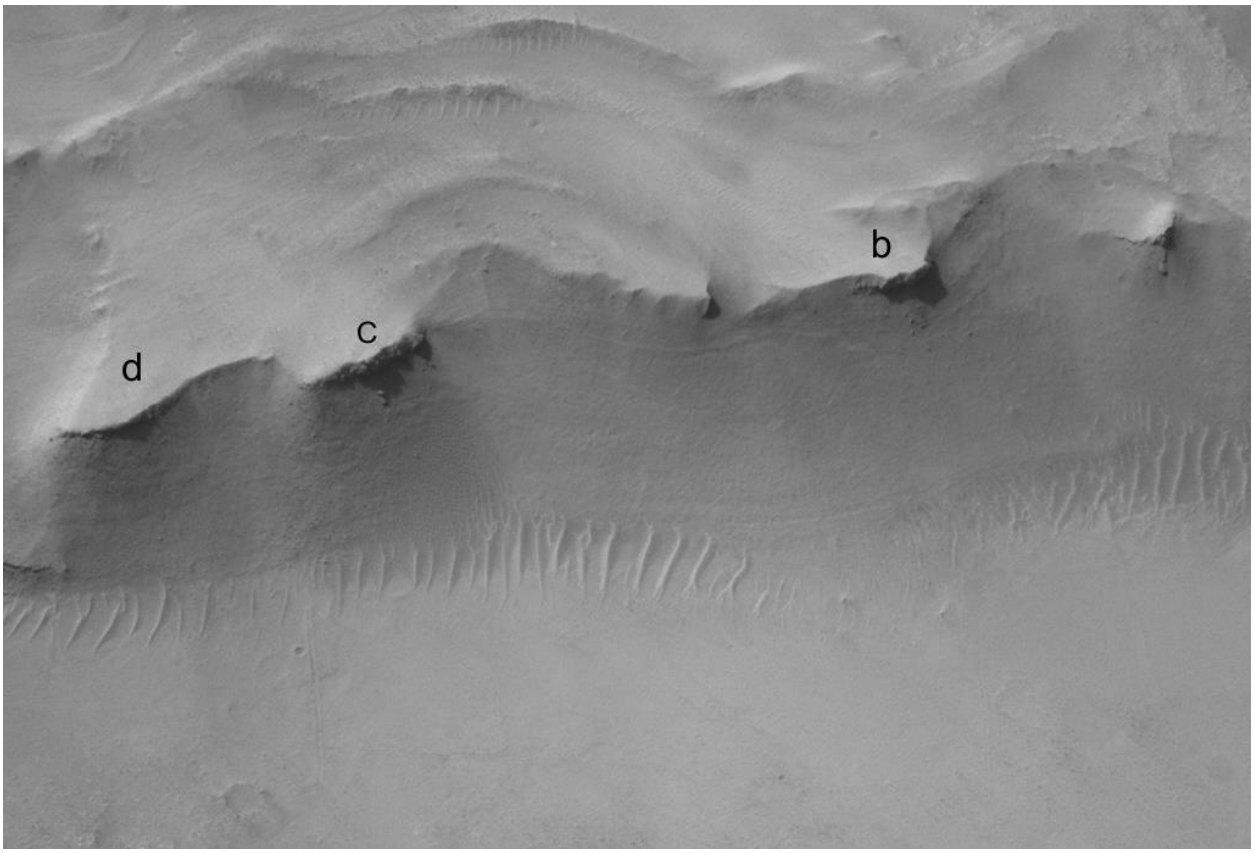

Figure S5: Entry, Descent and Landing (EDL) camera image of the delta front taken during the descent. The image highlights the talus and the presence at a similar elevation of three of the scarps that have subsequently been observed from the ground (Fig. 1, S4). Scarp b is approximately 15 m high and 70 m long and was the focus of the RMI mosaic (Fig. 4 and S4) while scarps c and d have been observed by Mastcam-Z only (Fig. 1). Orientation of the top of the image toward northwest. Image number RDC_00000005_000_003893_raw.

Figure S6: Clasts measured for clast size distribution. Close-up showing the boulder conglomerate of unit a2 (Fig. 3, S3) with average dimensions measured for 333 clasts. White lines indicate where the measurements of long and short axes have been made. See supplementary text for further explanation.

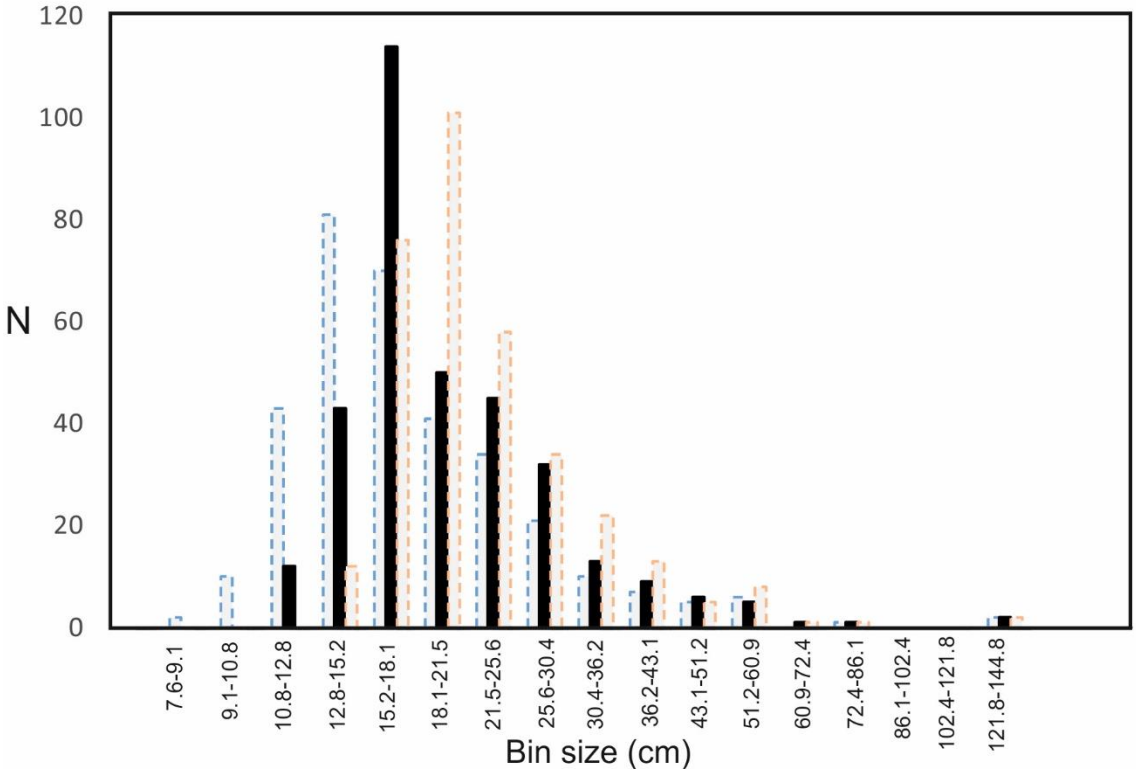

Figure S7: Histogram of the boulder size distribution. Black bars correspond to the plot of clast size (same distribution as in cumulative plot of Figure 3E) per bin size using Wentworth grain size scale (*75*). Lower and upper bounds are denoted with dotted blue bars and dotted red bars, respectively. N is the number of clasts per bin (for a total of 333).

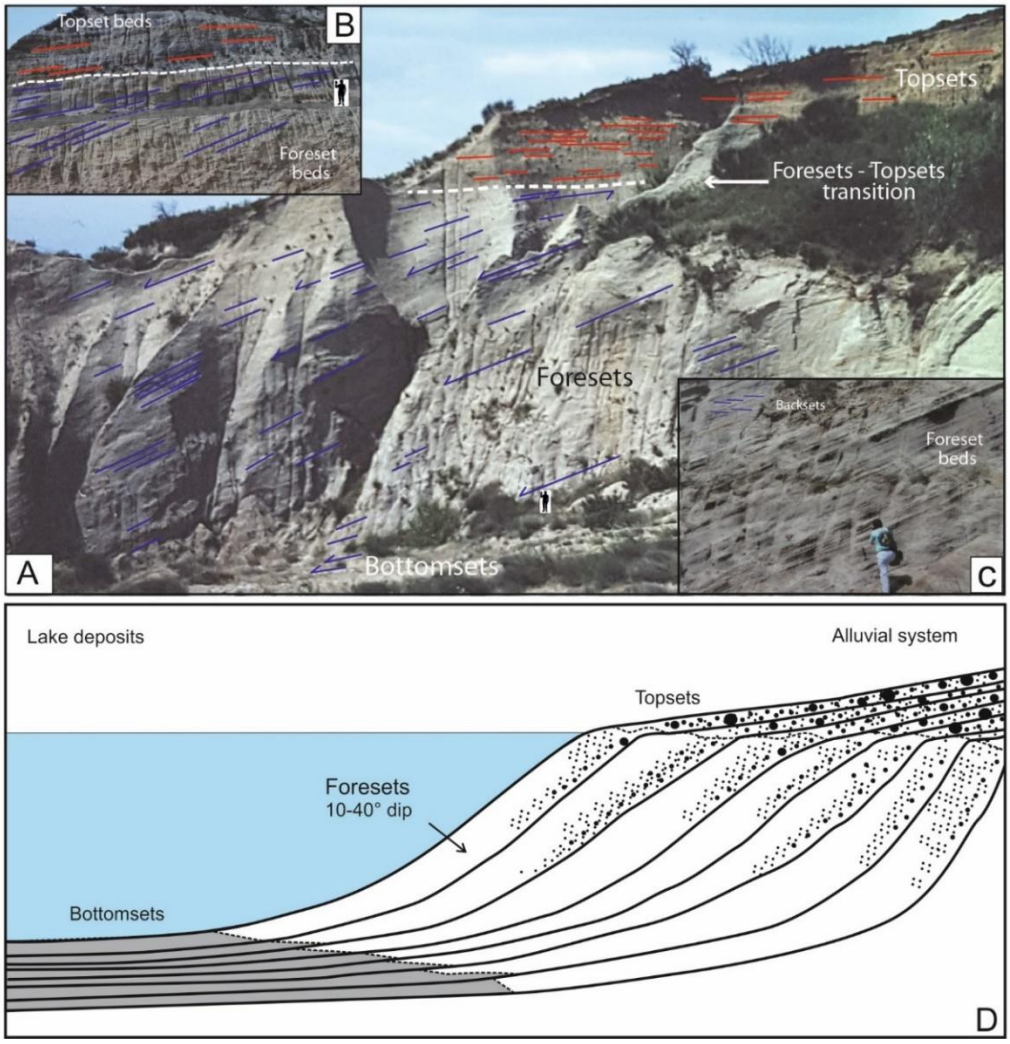

Fig. S8. **Geometry of Gilbert-type fan deltas.** (A) General view of the Pliocene of Bente Farine Quarry, Néfiach area, Pyrénées-Orientales, France (images taken in 1993) showing a Gilbert delta with the typical tripartite structure of a Gilbert fan delta (topsets, foresets, bottomsets) marked by depositional slopes that dip steeply (general linear slope of 22° to the left). The section shown is subparallel to the direction of progradation and the vertical development of the foreset section is approximately 25 m (human silhouette for scale). (B) Topset beds consisting of crudely stratified, gently inclined floodplain to soil heterolithic deposits and sheetflood to braided river conglomerates. The topset–foreset boundary is transitional, producing a sigmoidal stratal termination pattern. The toplap-type foresets–topsets surface marks the transition from marine (foresets) to continental (topsets) depositional facies. (C) Coarse-grained foresets with well-defined bedding and steep primary dips to the left (22°). The (lower slope) foreset beds have a mostly planar geometry, with high lateral persistence. They are composed of coarse sandstones and resistant, clast-supported, poorly-sorted pebbly sandstones. Note sets of upslope-dipping cross-strata that occur as thin, sub-horizontal sand beds. (D) Sketch of a Gilbert delta on Earth (after *19*). To the right, a fluvial system (coarse material, topsets) transitions gradually into steeply inclined foresets with locally coarse, generally finer-grained material, which transition into bottomsets comprising only fine-grained material (mudstones, in gray tone) at the lake bottom.

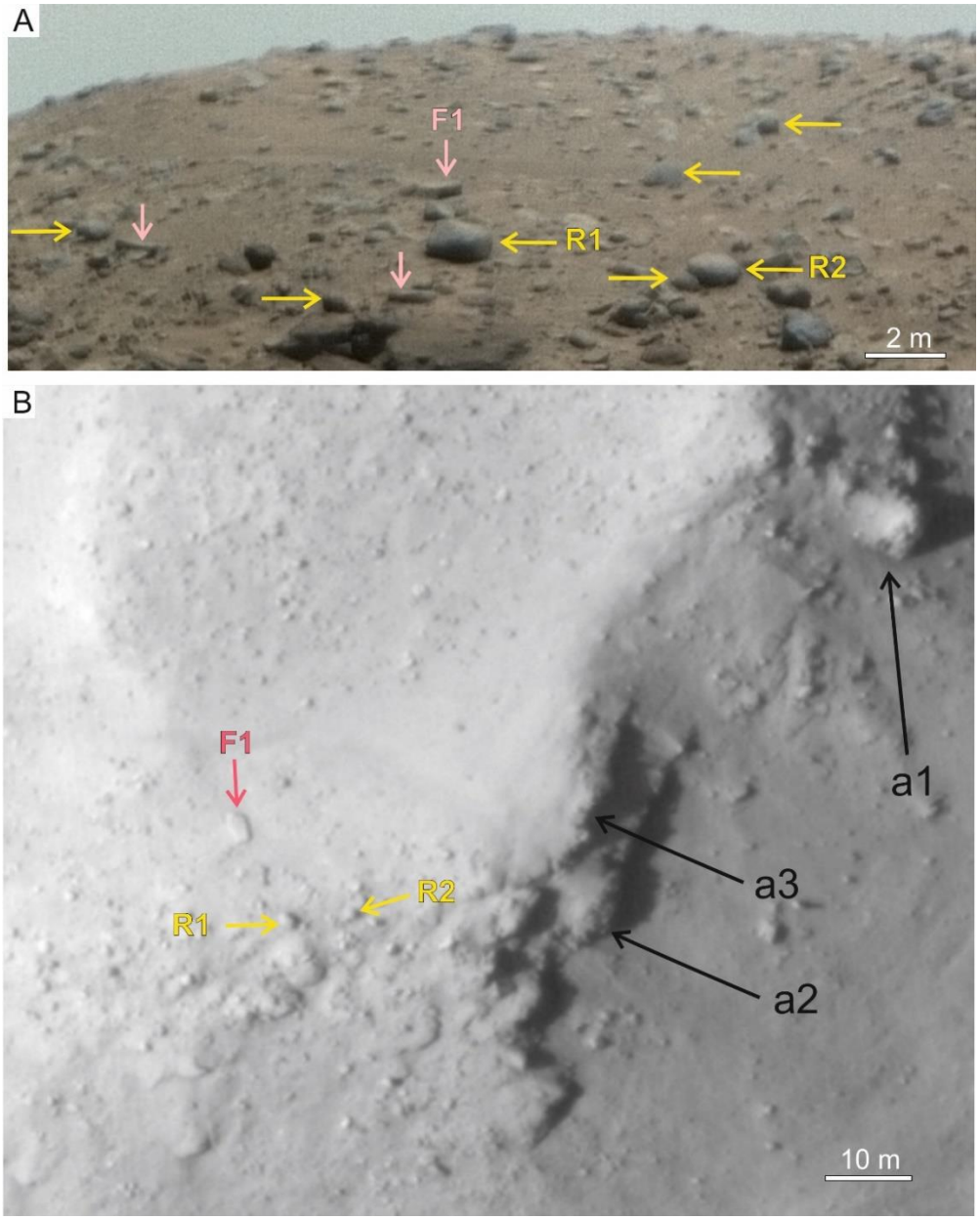

Figure S9: Comparison between orbital data and ground observations. HiRISE image (B) of the topmost part of the RMI mosaic of sol 26 (A). Arrows on the orbital images indicate sedimentary bodies a1 to a3 visible in Fig. 3. Many boulders observed in the RMI image (black arrows) are well-rounded with the same massive shape and gray tone as boulders observed within a2 and a3 (Fig. 3). This suggests a similar origin, likely weathered and eroded conglomerate beds. Rounded boulders R1 and R2 have been localized on the orbital image. A few lighter-toned, angular, flat-topped blocks are distinct from boulders such as F1, are indicated in both the RMI and the orbital image (white arrows). These angular blocks are interpreted as portions of cemented sandstones weathered from units similar to a3.

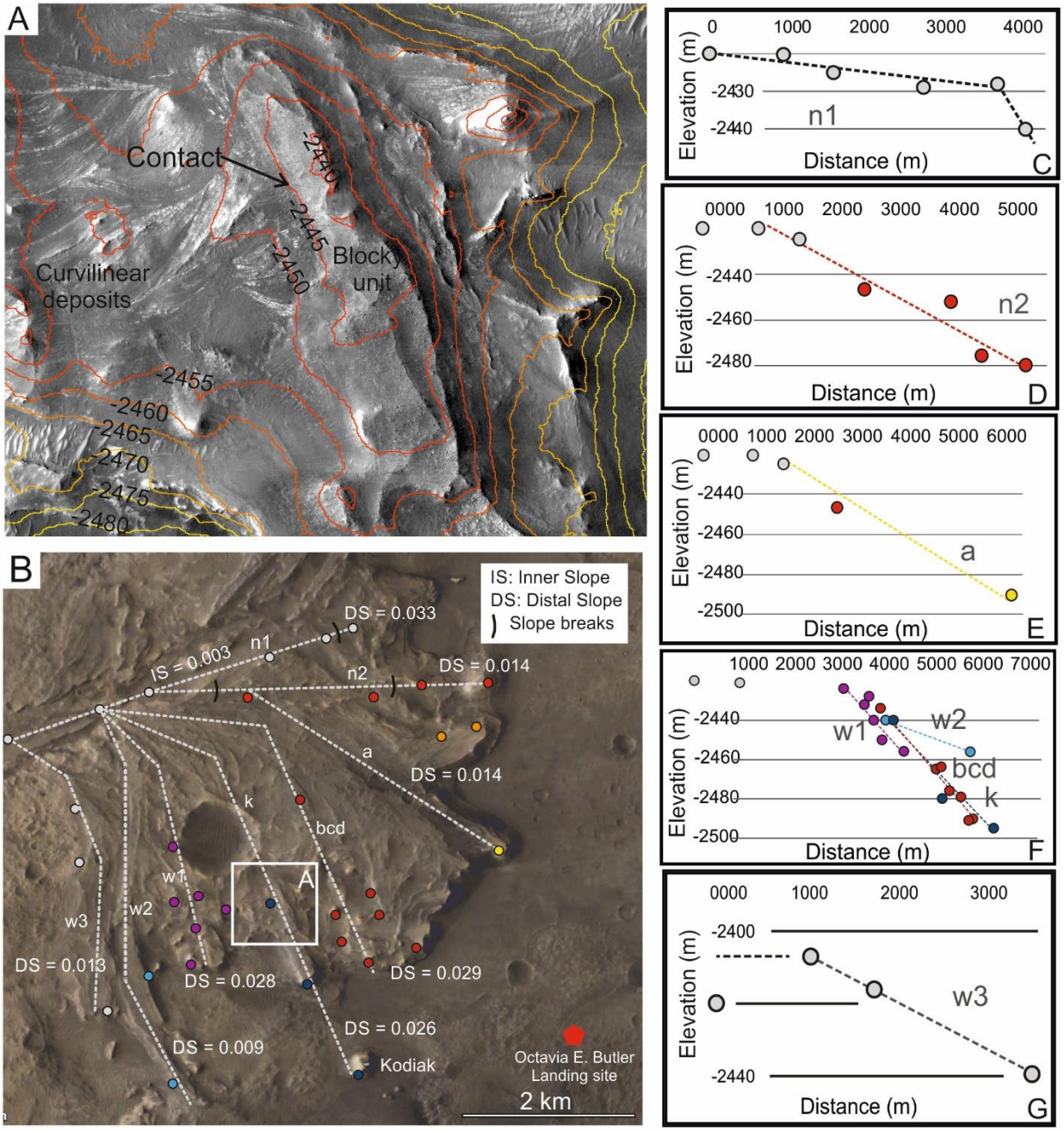

Figure S10: **Measurements of the basal slope of the Delta Blocky Unit**. (A) Example of a contact observed on a HiRISE image between the Delta Curvilinear Truncated Layered Deposits and Delta Blocky units mapped on the geological map (Fig. S1, *15*). Location of the close-up shown with a white rectangle in (B). (B) HiRISE image with profiles (dotted lines) from which the basal slope of the Delta Blocky Unit (*15*) has been extracted using each visible contact (color dots). (C) to (G) Basal slope profiles of the between the base of the Delta Blocky Unit and underlying deposits extrapolated from the contacts observed.

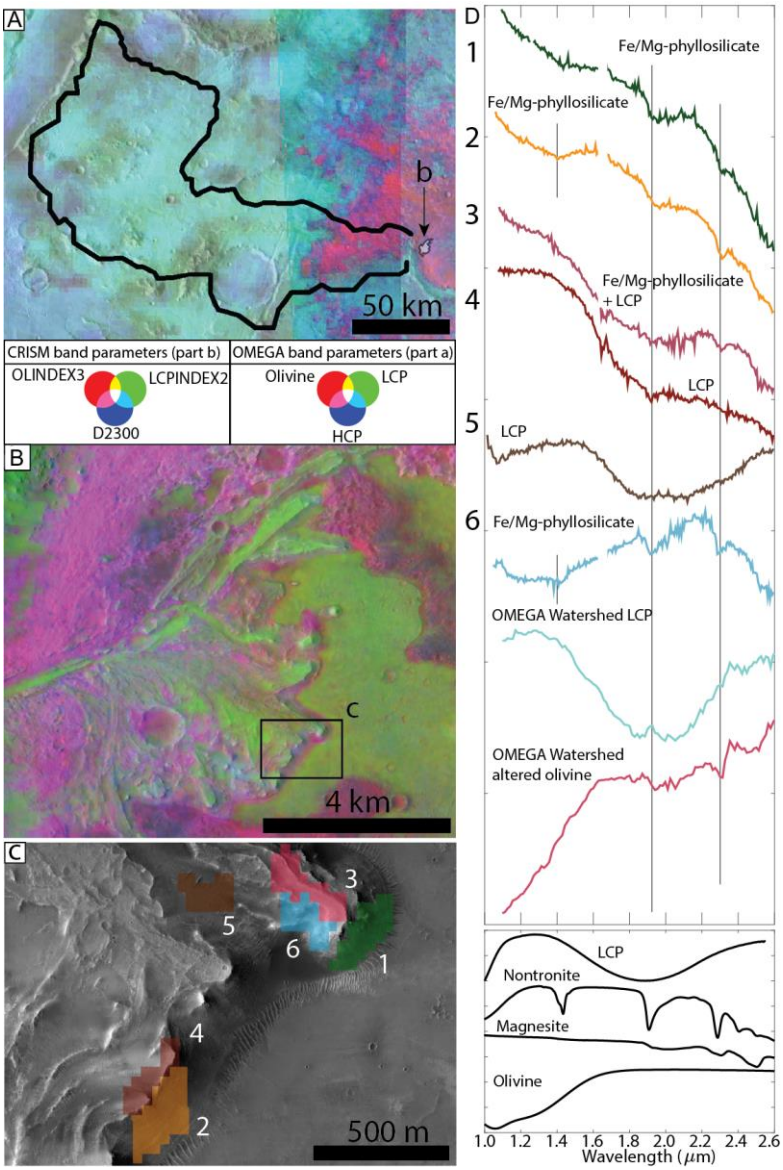

Figure S11: Mineralogy of the delta and watershed of Jezero crater from orbital data. (A) OMEGA mosaic of observations from Mars Express spacecraft orbits 0422 and 2272 of Neretva Vallis basin. The arrow indicates Jezero crater western delta. OLINDEX3, LCPINDEX2, and D2300 are the names of band parameters (*64*). OLINDEX3 and LCPINDEX2 highlight areas with spectral features consistent with olivine and LCP, respectively. D2300 measures the depth of the 2.3 μm absorption band, which is consistent with the presence of Fe/Mg-phyllosilicates. (B) CRISM image HRL000040FF color composite of the Jezero delta showing that LCP (in green) is widespread on the top of the delta. (C) Enlarged image of the delta front and location of the CRISM spectra 1 to 6 displayed in (D). (D) Upper diagram: spectra 1 to 6 are from CRISM normalized by nearby spectrally neutral material (*64*). Both OMEGA spectra are also normalized to nearby spectrally neutral material, and were acquired from LCP-bearing terrains and olivine-bearing terrains of the watershed displayed in (A). The lower part of the diagram are four laboratory infrared spectra for reference obtained from the Keck/NASA Reflectance Experiment Laboratory Spectral Library.

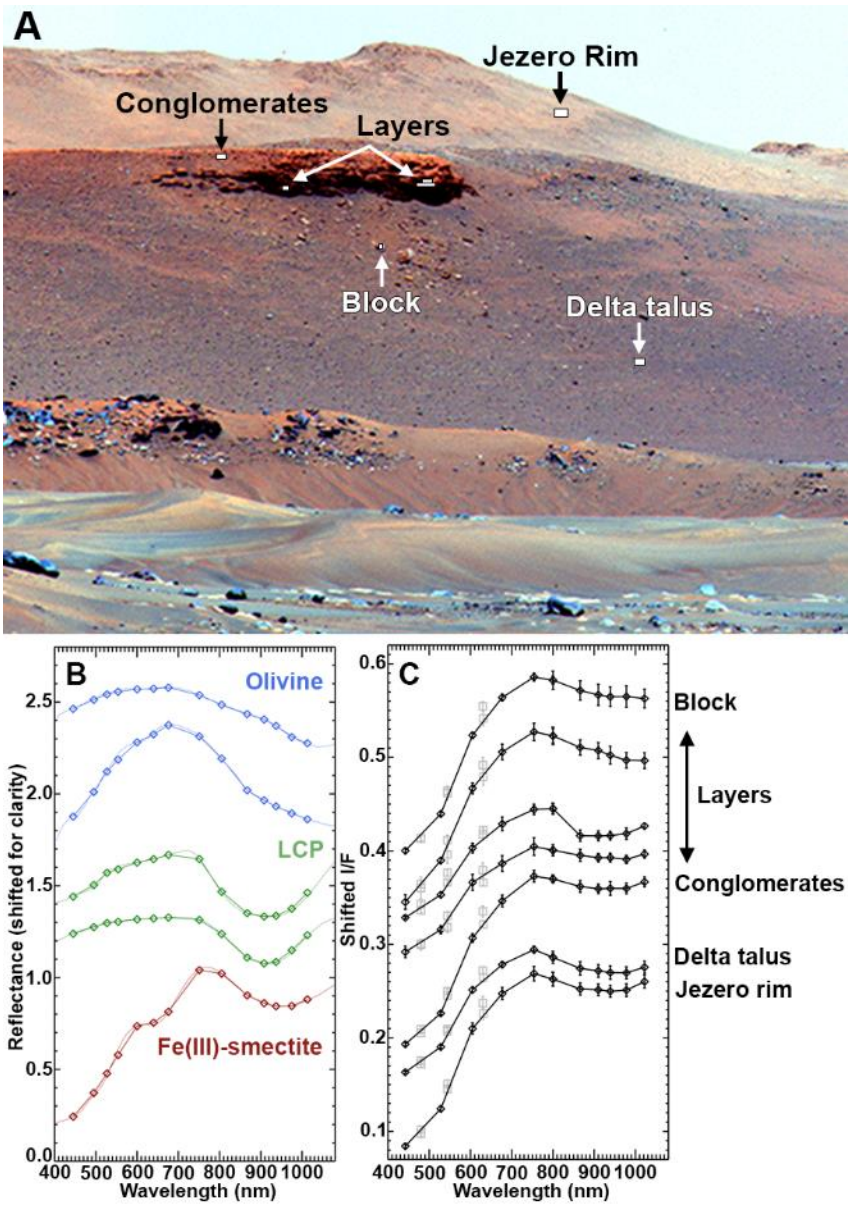

Figure S12: **Composition of the delta front from rover observations.** Mastcam-Z multispectral image of the delta front scarp "b" shown in SuperCam RMI in Fig. 4 and S4 (Tab. S1). (A) Enhanced color image from 754, 528, 442 nm narrowband filters (L256) showing from back to front: Jezero crater rim, delta scarp, and landing site terrain. (B) Laboratory spectra from the United States Geological Survey database (*76)* convolved with Mastcam-Z filters. (C) Mastcam-Z *I/F* spectra from locations indicated in (A). Black points indicate narrowband filters and gray points indicate broadband Bayer filters. The Jezero rim shows an absorption band near 900 nm consistent with LCP in the Noachian basement, which is similar to the delta conglomerates, talus, and some thinly bedded layers. Nonetheless, the layers are of variable composition, and some layers and blocks on the slope below show strong blue slopes with long wavelengths potentially consistent with olivine.

Table S1: Mastcam-Z image details. LTST = local true solar time. Individual image files can be downloaded at the Planetary Data System in the folder of the Mastcam-Z dataset: https://pds-imaging.jpl.nasa.gov/data/mars2020/mars2020_mastcamz/data_asu/rad/

Figures	Sequence	Sol	File name on Planetary Data System	Sequence Start-End (LTST)	Filter(s) Used
1b S2	zcam08022	63	0063/ZL0_0063_0672518294_292RAD_N0032046ZCAM08022_1100LUA02.IMG	08:29-08:31	L0
1c-g	zcam08103	57	0057/ZL0_0057_0671994449_364RAD_N0032046ZCAM08103_110085A02.IMG 0057/ZL0_0057_0671994465_364RAD_N0032046ZCAM08103_110085A02.IMG 0057/ZL0_0057_0671994477_364RAD_N0032046ZCAM08103_110085A02.IMG 0057/ZL0_0057_0671994496_364RAD_N0032046ZCAM08103_110085A02.IMG 0057/ZL0_0057_0671994508_364RAD_N0032046ZCAM08103_110085A02.IMG 0057/ZL0_0057_0671994520_364RAD_N0032046ZCAM08103_110085A02.IMG 0057/ZL0_0057_0671994532_364RAD_N0032046ZCAM08103_110085A02.IMG 0057/ZL0_0057_0671994544_364RAD_N0032046ZCAM08103_110085A02.IMG 0057/ZL0_0057_0671994556_364RAD_N0032046ZCAM08103_110085A02.IMG 0057/ZL0_0057_0671994570_364RAD_N0032046ZCAM08103_110085A02.IMG 0057/ZL0_0057_0671994584_364RAD_N0032046ZCAM08103_110085A02.IMG 0057/ZL0_0057_0671994597_364RAD_N0032046ZCAM08103_110085A02.IMG	10:10-11:16	L0
S3	zcam08002	26	0026/ZL0_0026_0669245316_186RAD_N0030792ZCAM08002_1100LUA02.IMG 0026/ZL0_0026_0669245431_186RAD_N0030792ZCAM08002_1100LUA02.IMG	11:09-11:11	L0
S4 S12	zcam03113	54	0054/ZL0_0054_0671729980_150RAD_N0032046ZCAM03113_1100LUA02.IMG 0054/ZL2_0054_0671730058_146RAD_N0032046ZCAM03113_1100LUA02.IMG 0054/ZL5_0054_0671730113_146RAD_N0032046ZCAM03113_1100LUA02.IMG 0054/ZL6_0054_0671730136_146RAD_N0032046ZCAM03113_1100LUA02.IMG	11:23-11:27	L0 L256

Table S2: SuperCam/Remote Micro-Imager image details. LTST = local true solar time. Individual files can be downloaded at the Planetary Data System in the folder of the RMI dataset: https://pds-geosciences.wustl.edu/m2020/urn-nasa-pds-mars2020_supercam/data_radcal_rmi/

Figures	Sequence	Sol	File name on Planetary Data System	Sequence Start (LTST)	Distance (m)
2, S2	scam01063	63	sol_00063/scam_0063_0672517268_221_ci__scam01063_ld_kodiak_63_____01p01.fits sol_00063/scam_0063_0672517353_179_ci__scam01063_ld_kodiak_63_____02p01.fits sol_00063/scam_0063_0672517438_141_ci__scam01063_ld_kodiak_63_____03p01.fits sol_00063/scam_0063_0672517523_139_ci__scam01063_ld_kodiak_63_____04p01.fits sol_00063/scam_0063_0672517735_139_ci__scam01063_ld_kodiak_63_____05p01.fits sol_00063/scam_0063_0672517820_345_ci__scam01063_ld_kodiak_63_____06p01.fits sol_00063/scam_0063_0672517906_140_ci__scam01063_ld_kodiak_63_____07p01.fits sol_00063/scam_0063_0672517991_142_ci__scam01063_ld_kodiak_63_____08p01.fits sol_00063/scam_0063_0672518076_141_ci__scam01063_ld_kodiak_63_____09p01.fits sol_00063/scam_0063_0672518161_140_ci__scam01063_ld_kodiak_63_____10p01.fits	08:05-08:28	2240
3, S3	scam02026	26	sol_00026/scam_0026_0669244563_180_ci__scam02026_ld_delta_26a_____01p01.fits sol_00026/scam_0026_0669244652_160_ci__scam02026_ld_delta_26a_____02p01.fits sol_00026/scam_0026_0669244741_149_ci__scam02026_ld_delta_26a_____03p01.fits sol_00026/scam_0026_0669244830_220_ci__scam02026_ld_delta_26a_____04p01.fits sol_00026/scam_0026_0669244920_177_ci__scam02026_ld_delta_26a_____05p01.fits	11:22-11:32	2200
4, S4	scam01054	54	sol_00054/scam_0054_0671728791_140_ci__scam01054_ld_delta_54a_____01p01.fits sol_00054/scam_0054_0671728989_466_ci__scam01054_ld_delta_54a_____02p01.fits sol_00054/scam_0054_0671729188_479_ci__scam01054_ld_delta_54a_____03p01.fits sol_00054/scam_0054_0671729188_479_ci__scam01054_ld_delta_54a_____04p01.fits sol_00054/scam_0054_0671729682_387_ci__scam01054_ld_delta_54a_____05p01.fits	10:59-11:20	2230

Table S3: Discharge rates estimated for unit a2. Velocity (V in m s^{-1}) in and discharge rates (Q in m^3 s^{-1}) according to equations (S2) and (S5) to (S7). Heights are deduced from terrestrial scaling laws (*14*) assuming various widths, except for the upper bound at 7 m estimated from direct observations of a2. Slopes values are minimum and maximum (*14*). D_{50} and D_{84} were taken as minima and maxima, respectively, to provide minimum and maximum estimates from equations (S2) and (S5).

Width (m)	**Height (m)**	**Slope**	***D*$_{50}$ (m)**	***D*$_{84}$ (m)**	***V* (S2)**	***Q* (S2)**	***V* (S5)**	***Q* (S5)**	***V* (S6)**	***Q* (S6)**	***V* (S7)**	***Q* (S7)**
30	1.55	0.012	0.142	0.281	1.63	76	1.98	92	2.97	137	1.91	88
50	2.17	0.012	0.142	0.281	1.92	207	2.62	284	2.97	322	1.91	207
50	2.17	0.029	0.142	0.281	2.34	253	4.08	441	2.89	313	1.91	207
100	3.40	0.029	0.142	0.281	2.89	989	5.85	2003	2.89	990	1.91	654
50	7	0.029	0.142	0.281	3.66	1281	8.64	3023	2.89	1011	1.91	668